MASTER'S THESIS

Wheel-terrain contact angle estimation for planetary exploration rovers

Ria Vijayan

Master of Science in Space Science and Technology

Luleå University of Technology
Department of Computer Sciences, Electrical and Space Engineering

LULEÅ UNIVERSITY OF TECHNOLOGY

MASTER THESIS IN SPACE SCIENCE AND TECHNOLOGY

Wheel-terrain contact angle estimation for planetary exploration rovers

Ria Vijayan
Luleå University of Technology
Division of Space Technology
981 28 Kiruna, Sweden

performed at
Deutsches Zentrum für Luft- und Raumfahrt

13 August 2018

Supervisor: Stefan Barthelmes (DLR)

Examiner: Anita Enmark (LTU)

Abstract

During space missions, real time tele-operation of a rover is not practical because of significant signal latencies associated with inter planetary distances, making some degree of autonomy in rover control desirable. One of the challenges to achieving autonomy is the determination of terrain traversability. As part of this field, the determination of motion state of a rover on rough terrain via the estimation of wheel-terrain contact angles is proposed.

This thesis investigates the feasibility of estimating the contact angles from the kinematics of the rover system and measurements from the onboard inertial measurement unit (IMU), joint angle sensors and wheel encoders. This approach does not rely on any knowledge of the terrain geometry or terrain mechanical properties.

An existing framework of rover velocity and wheel slip estimation for flat terrain has been extended to additionally estimate the wheel-terrain contact angle along with a side slip angle for each individual wheel, for rough terrain drive. A random walk and a damped model are used to describe the evolution of the contact angle and side slip angle over an unknown terrain. A standard strapdown algorithm for the estimation of attitude and velocity from IMU measurements, is modified to incorporate the 3D kinematics of the rover in the implementation of a nonlinear Kalman filter to estimate the motion states. The estimation results from the filter are verified using tests performed on the ExoMars BB2. The obtained contact angle estimates are found to be consistent with the reference values.

Keywords: *Contact Angle, Side Slip Angle, Nonlinear Kalman Filter, Differential Kinematics, ExoMars BB2, Planetary Exploration Rovers*

I dedicate this thesis to my parents

Acknowledgements

I would like to express my deepest gratitude to my supervisor Mr. Stefan Barthelmes for his meticulous guidance and continuous support through the course of this master thesis. I would also like to place on record my indebtedness to DLR Oberpfaffenhofen and all the colleagues for the cordial atmosphere of work. The project would not have been possible without the mobility grant provided by Erasmus+ and Université Paul Sabatier, Toulouse. I'm grateful for the support offered to me by my professor Ms Anita Enmark and the administration at Luleå Tekniska Universitet, Kiruna.

Oberpfaffenhofen, 13 August 2018
Ria Vijayan

Table of Contents

List of Tables

List of Figures

Nomenclature

$(\bullet)^a_{a,b}$	Quantity $(\bullet)$ in frame $\{\mathrm{b}\}$ wrt frame $\{\mathrm{a}\}$ expressed in frame $\{\mathrm{a}\}$
β	Wheel side slip angle
$\boldsymbol{\omega}$	Rotation vector or angular velocity
γ	Wheel-terrain contact angle
n	Index for wheel
ω_{w}	Wheel rate
ϕ	Roll
ψ	Yaw
$\mathbf{a}$	Acceleration
$\mathbf{f}$	Specific force
$\mathbf{f}()$	State transition function
$\mathbf{g}$	Gravity vector
$\mathbf{h}()$	Measurement function
$\mathbf{J}$	Jacobian matrix
$\mathbf{n}_{(\bullet)}$	Noise associated with quantity $(\bullet)$
$\mathbf{q}$	DOF vector containing joint rate and additional DOFs defined by various slips or turn rate

$\mathbf{r}$	Position vector
$\mathbf{R}_\bullet$	Rotation matrix describing rotation about $(\bullet)axis$
$\mathbf{T}$	Transformation matrix
$\mathbf{u}_m$	Measurement input vector
$\mathbf{u}_p$	Process input vector
$\mathbf{v}$	Velocity
$\mathbf{x}$	State vector
$\mathbf{y}$	Measurement vector
Θ	Orientation vector
θ	Pitch
A	Damping parameter for damped model
k	k^{th} time step in a discretized model
r_{w}	Radius of wheel
s	Wheel slip
t_s	Filter time step
$\mathbf{R}_a^b$	Rotation matrix transforming frame a to frame b
q_b	Bogie rotation
q_s	Steering rotation

Abbreviations

ESA	-	European Space Agency
NASA	-	National Aeronautics and Space Administration
DLR	-	Deutsches Zentrum für Luft- und Raumfahrt
PEL	-	Planetary Exploration Lab
BB2	-	Breadboard 2
IMU	-	Inertial Measurement Unit
3D	-	3 Dimension
DH	-	Denavit-Hartenberg
EKF	-	Extended Kalman filter
UKF	-	Unscented Kalman filter
DOF	-	Degree of Freedom
CoG	-	Center of Gravity
ODE	-	Ordinary Differential Equation
FL	-	Front Left (wheel)
ML	-	Middle Left (wheel)
RL	-	Rear Left (wheel)
RR	-	Rear Right (wheel)
MR	-	Middle Right (wheel)
FR	-	Front Right (wheel)
RMS	-	Root Mean Square

Chapter 1

Introduction

The use of rovers for planetary exploration has become an attractive solution to getting scientific payload into territories previously not investigated. *Lunokhod 1*, a Soviet rover on the moon launched in 1970, was the first successfully operated remote-controlled rover on an extra-terrestrial surface. *Sojourner*, part of NASA's Mars Pathfinder mission, became the first rover to be successfully operated on another planet. The ExoMars rover by ESA is scheduled to be launched in 2020. Consequently, the past few decades have seen a lot of research and development in the design of rover systems and modelling of their system dynamics and control. The discussion in this thesis is limited to *wheeled* rovers, although rovers in general could have *legs*, skis, or other mechanisms for locomotion.

1.1 Motivation

The need for full or partial autonomy of rover systems is motivated by signal latency between Earth-based ground station and rover telecommunication systems, which can have detrimental consequences for the rover in times of emergency. For example, if the rover were approaching a cliff, the time it takes this information to be transmitted to an Earth-based ground station and a response relayed back to a rover, limits the scope for implementation of a contingency plan. Signal latency is an inherent drawback for any interplanetary mission and therefore calls for autonomy in rover operations.

A rover with a good degree of autonomy attained by the monitoring of several system indicators could minimize the risk of it getting trapped in irrecoverable situations. Terrain traversability is one of the challenges that, when not well deter-

mined, can hamper with the mobility of a rover. This, in turn, can compromise its most essential and distinguishing advantage over a space exploration module like a lander. Traversability can be determined from characterization of terrain properties that affect traction, like soil cohesion and friction. Traversability can also be determined by characterizing the terrain geometry to know if it is smooth, rocky or non-geometric like loose sand. The latter is a problem encountered on Martian terrain, for example by NASA's *Opportunity*. Stuck in loose sand, it experienced excessive slip and sinking of the wheels.

In order to tackle the challenges associated with terrain traversability, several approaches could be adopted. For example, the mechanical design of the rover mechanism could be improved for better manoeuvrability, the center of mass of the rover could be actively redistributed (Iagnemma et al., 2000), the design of wheel and grousers could be improved for better traction, the motion control could be improved by optimizing wheel torques and speeds to minimize wheel slip, and so on. In this thesis one of the challenges to achieving autonomy is dealt with, which is to understand the motion state of a rover better by means of estimating the wheel-terrain contact angles.

1.2 Research problem

For motion control, the motion state of a rover has to be defined by some parameters and/or variables. From a dynamics perspective, one of the possibilities is to look at the forces, stresses and torques developed at the wheel-terrain interface. This would help to know how much resistance force and torque needs to be overcome for locomotion. This would require the installation of heavy and expensive force-torque sensors and/or elaborate dynamic modelling and estimation of the contact forces. Furthermore, this may require the knowledge of certain soil parameters, which are unknown or difficult to estimate for extra-terrestrial terrain.

From a kinematics perspective, the knowledge of position, velocity and acceleration of the rover would help define the motion state of the rover. A rover on an extra-terrestrial surface has no access to navigation satellite systems to track its exact location and thereby determine its speed of travel. The position of the rover is commonly determined by visual odometry. However it is a computationally expensive approach to process the data from the onboard cameras. The pose of the rover can be estimated from measurements of the IMU, star sensors, sun sensors and/or other sensors onboard. Weight, expense and implementation difficulties of sophisticated sensors and limited computational capacity of onboard processors are some of the factors that necessitate simple and reliable solutions to determin-

ing the motion state of a rover. Other motion state indicators include longitudinal and lateral wheel slips, vehicle skid etc. This thesis focuses on one of the motion state indicators – the contact angle of a wheel with terrain, which is related to the inclination of the terrain and gives insight into the unevenness of wheel climb on rough terrain. The knowledge of contact angles could be used to better optimize wheel motion control and thereby minimize wheel slip.

The contact angle, as defined in this thesis, captures the vertical component of wheel velocity (introduced in Section 5.1). By introducing a contact angle, it accounts for possible vertical motion of the wheel, unlike the case of smooth terrain drive where only longitudinal wheel motion in the wheel frame is considered. The existing framework of estimation at DLR, estimates the rover velocity and wheel slips for a smooth terrain, assuming contact angles to be zero. In order to extend this framework to the estimation of rover velocity and wheel slip when the wheels have non-zero contact angles on a rough terrain, an estimation of the contact angles themselves is required to be developed.

1.3 Research goal

The scope of research in this thesis is to investigate the feasibility of estimating the wheel-terrain contact angles from purely the rover 3D kinematics and measurements from the IMU, joint angle sensors and wheel encoders. No prior knowledge of the terrain, for example an elevation map or soil properties, are used for the estimation. This thesis extends the estimation of rover velocity and wheel slip for rough terrain by modifying the existing framework of estimation for smooth terrain with the estimation of contact angles.

1.4 Approach

First the differential kinematics of the rover from the existing framework is elaborated in Chapter 4. In this context the wheel-terrain contact angle is defined, modelled and incorporated into the system model to account for vertical wheel motion of a rover travelling on uneven or rough terrain. Additionally a wheel side slip angle, which captures lateral motion of the wheels, is similarly defined, modelled and introduced into the system model. With the introduction of both the contact and side slip angle the wheel velocity is captured in three dimensions. Two models are developed which account for wheel motions in addition to the longitudinal direction. First, a *contact angle model*, which accounts for additional vertical wheel motion. Second, a *contact & side slip angle model* which accounts for additional vertical and lateral wheel motions. The rover motion in this thesis is captured

by the rover velocity, wheel slip, contact angles and side slip angles. A standard strapdown algorithm which is used for estimating attitude and rover velocity, is modified to incorporate the 3D differential kinematics of the rover for the estimation of the aforementioned motion states using a nonlinear Kalman filter. Lastly the implementation and results of the filter are verified against tests conducted on the ExoMars BB2 at the Planetary Exploration Lab (PEL), DLR.

Autonomy of robot systems used in planetary exploration involves its guidance, navigation and control. The more reliable the estimates of the states of the system are, the more robust the controller which guides the rover can be. With reliable estimates of the contact angles (and side slip angles), the rover velocity and wheel slip estimation for rough terrain is developed. The three topics broadly covered in the thesis are :

- extension of the existing differential kinematics of the rover
- definition and modelling of contact angle and side slip angle
- extension of existing nonlinear Kalman filter framework for estimation of contact angles (and side slip angles).

1.5 Document Structure

Chapter 1 – Introduction
This chapter describes the motivation, research problem and objective of the thesis, and the brief outline of the approach used to solve the problem.

Chapter 2 – Theoretical background
This chapter briefly describes the mathematical concepts on which the differential kinematics and the filter algorithm are based.

Chapter 3 – State of the Art
This chapter brings the reader up to date on the relevant research that has been conducted in the topics of rover kinematics, development/estimation of wheel-terrain contact angle and estimation filter theory.

Chapter 4 – Velocity and slip estimator for smooth terrain
This chapter details the existing framework of estimation for rover velocity and wheel slip on smooth terrain.

Chapter 5 – Extension of estimator for uneven terrain
This chapter defines the contact angle and side slip angle and describes the extension of the filter framework. A short discussion on the nonlinearity of the entire system model is also presented.

Chapter 6 – Results and verification
This chapter presents the results and analysis of the filter from the *contact angle model* and *contact & side slip angle model* for hypothetical scenarios and real tests conducted on the ExoMars rover at PEL.

Chapter 7 – Conclusions and Future Work
This chapter summarizes the thesis, conclusions from the results and suggests possible future work.

Chapter 2

Theoretical Background

Some of the basics required to model the system and estimate the states are covered in this chapter. For all notations refer to the **Nomenclature** listed before Chapter 1.

2.1 Coordinate transformation

Any orientation can be expressed as a sequence of three consecutive rotations according to Euler's rotation theorem (Marcel J, 1997). The basic rotations are given by Eq. (2.1).

$$\begin{aligned}
\mathbf{R_x}(\phi) &= \begin{bmatrix} 1 & 0 & 0 \\ 0 & \cos\phi & -\sin\phi \\ 0 & \sin\phi & \cos\phi \end{bmatrix} \\
\mathbf{R_y}(\theta) &= \begin{bmatrix} \cos\theta & 0 & \sin\theta \\ 0 & 1 & 0 \\ -\sin\theta & 0 & \cos\theta \end{bmatrix} \\
\mathbf{R_z}(\psi) &= \begin{bmatrix} \cos\phi & -\sin\phi & 0 \\ \sin\phi & \cos\phi & 0 \\ 0 & 0 & 1 \end{bmatrix}
\end{aligned} \tag{2.1}$$

Given 2 frames $\{\mathbf{A}\}$ and $\{\mathbf{B}\}$ as shown in Fig. 2.1 the rotation matrix that gives the orientation of frame $\{\mathbf{A}\}$ with respect to frame $\{\mathbf{B}\}$ is given by Eq. (2.2). The rotation sequence XYZ is used to obtain the rotation matrix in Eq. (2.2) using Euler angles ψ, θ, ϕ for yaw, pitch and roll.

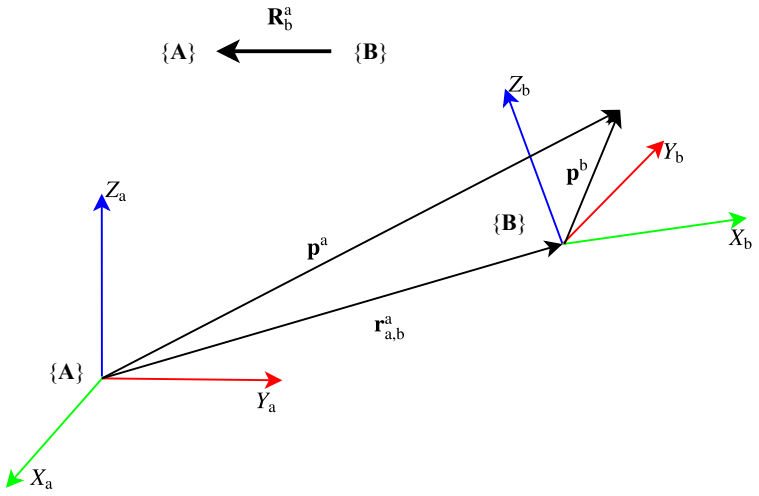

Figure 2.1: Coordinate transformation

$$\mathbf{R}^{a}_{b} = \mathbf{R_z}(\psi)\mathbf{R_y}(\theta)\mathbf{R_x}(\phi) =$$
$$\begin{bmatrix} \cos\psi\cos\theta & -\sin\psi\cos\phi+\cos\psi\sin\theta\sin\phi & \sin\psi\sin\phi+\cos\psi\sin\theta\cos\phi \\ \sin\psi\cos\theta & \cos\psi\cos\phi+\sin\psi\sin\theta\sin\phi & -\cos\psi\sin\phi+\sin\psi\sin\theta\cos\phi \\ -\sin\theta & \cos\theta\sin\phi & \cos\theta\cos\phi \end{bmatrix} \tag{2.2}$$

The vector $\mathbf{r}^{a}_{a,b}$ is the path along which frame $\{\mathbf{B}\}$ needs to be translated for its origin to coincide with that of frame $\{\mathbf{A}\}$. A point $\mathbf{p}^{b}$ expressed in frame $\{\mathbf{B}\}$ can be transformed to frame $\{\mathbf{A}\}$ as per Eq. (2.3).

$$\mathbf{p}^{a} = \mathbf{R}^{a}_{b}\mathbf{p}^{b} + \mathbf{r}^{a}_{a,b} \tag{2.3}$$

Some useful properties of orthogonal rotation matrices:

1. $\det \mathbf{R}^{a}_{b} = 1$
2. $\mathbf{R}^{b}_{a} = (\mathbf{R}^{a}_{b})^{-1} = (\mathbf{R}^{a}_{b})^{T}$
3. $\mathbf{R}^{a}_{c} = \mathbf{R}^{a}_{b}\mathbf{R}^{b}_{c}$
4. $\dot{\mathbf{R}}^{a}_{b} = \mathbf{R}^{a}_{b}[\boldsymbol{\omega}^{b}_{a,b}\times] = [\boldsymbol{\omega}^{a}_{a,b}\times]\mathbf{R}^{a}_{b}$

A homogeneous transformation matrix combines the rotation and translation between frames in a compact form.

$$\mathbf{T}_{\mathrm{b}}^{\mathrm{a}} = \begin{bmatrix} \mathbf{R}_{\mathrm{a}}^{\mathrm{b}} & \mathbf{r}_{\mathrm{a,b}}^{\mathrm{a}} \\ \mathbf{0} & 1 \end{bmatrix} \tag{2.4}$$

$$\begin{bmatrix} \mathbf{p}^{\mathrm{a}} \\ 1 \end{bmatrix} = \mathbf{T}_{\mathrm{b}}^{\mathrm{a}} \begin{bmatrix} \mathbf{p}^{\mathrm{b}} \\ 1 \end{bmatrix} \tag{2.5}$$

$$\mathbf{T}_{\mathrm{c}}^{\mathrm{a}} = \mathbf{T}_{\mathrm{b}}^{\mathrm{a}} \mathbf{T}_{\mathrm{c}}^{\mathrm{b}} \tag{2.6}$$

Using homogeneous coordinates the complete transformation is given by Eq. (2.5). Consecutive transformation between frames can be done using Eq. (2.6).

2.2 Denavit-Hartenberg convention

The Denavit-Hartenberg convention is the most commonly used convention for assigning coordinate frames to joints of robotic manipulators and defining the homogeneous transformation matrices between them with the help of 4 parameters per transformation. These parameters are called the DH parameters. The rules for defining the frames are:

- the z_i axis is taken along the axis of rotation of the i^{th} joint if it is a revolute joint, and along the sliding motion in the case of a prismatic joint.
- the x_i axis is defined along the common normal between the z_{i-1} and z_i axes and intersects both the z axes when extended.
- the origin of the joint frame is at the intersection of the joint's corresponding x_i and z_i axes.
- the y_i axis completes the triad

The 4 DH parameters used to map transformation between each joint are:

- θ_i - angle of rotation about z_{i-1} axis to align the x_{i-1} axis along the common normal (x_i)
- d_i - distance of translation along z_{i-1} axis to the common normal
- α_i - angle of rotation about transformed x_i axis to align the z_{i-1} axis along the z_i axis
- a_i - distance of translation along transformed x_i axis

With these 4 parameters systematically mapping each consecutive frame to the other, the transformation matrix for the end effector to base frame is given by Eqs. (2.7) and (2.8).

$$ {}^{0}\mathbf{T}_{n} = {}^{0}\,\mathbf{T}_{1}.{}^{1}\mathbf{T}_{2}...{}^{n-1}\mathbf{T}_{n} \tag{2.7} $$

$$ {}^{i-1}\mathbf{T}_{i} = \begin{bmatrix} \cos\theta_i & -\sin\theta_i\cos\alpha_i & \sin\theta_i\sin\alpha_i & a_i\cos\theta_i \\ \sin\theta_i & \cos\theta_i\cos\alpha_i & -\cos\theta_i\sin\alpha_i & a_i\sin\theta_i \\ 0 & \sin\alpha_i & \cos\alpha_i & d_i \\ 0 & 0 & 0 & 1 \end{bmatrix} \tag{2.8} $$

2.3 Jacobian matrix

The Jacobian matrix **J** is the matrix that gives the forward instantaneous kinematics of a chain of robotic links (Siciliano and Khatib, 2008). It relates the velocity of the end effector $\mathbf{v}^{0}_{0,\mathrm{n}}$ to the joint rates. The vector **q** contains all the joint DOFs involved in the kinematic chain between the base frame and end effector.

$$ \mathbf{v}^{0}_{0,\mathrm{n}} = \mathbf{J}(\mathbf{q})\dot{\mathbf{q}} \tag{2.9} $$

2.4 Euler angle differential kinematic equation

The angular velocity vector $\boldsymbol{\omega}^{\mathrm{b}}_{\mathrm{a,b}}$ of rotation of a body frame $\{\mathrm{B}\}$ with respect to frame $\{\mathrm{A}\}$ can be written as (Marcel J, 1997)

$$ \boldsymbol{\omega}^{\mathrm{b}}_{\mathrm{a,b}} = \omega_x\hat{\mathbf{x}}_{\mathrm{b}} + \omega_y\hat{\mathbf{y}}_{\mathrm{b}} + \omega_z\hat{\mathbf{z}}_{\mathrm{b}} $$

$$ \boldsymbol{\omega}^{\mathrm{b}}_{\mathrm{a,b}} = \mathbf{R}_{\mathbf{x}}(\phi)\mathbf{R}_{\mathbf{y}}(\theta)\mathbf{R}_{\mathbf{z}}(\psi)\begin{bmatrix}0\\0\\\dot{\psi}\end{bmatrix} + \mathbf{R}_{\mathbf{x}}(\phi)\mathbf{R}_{\mathrm{y}}(\theta)\begin{bmatrix}0\\\dot{\theta}\\0\end{bmatrix} + \mathbf{R}_{\mathbf{x}}(\phi)\begin{bmatrix}\dot{\phi}\\0\\0\end{bmatrix} \tag{2.10} $$

$$ \begin{bmatrix}\dot{\psi}\\\dot{\theta}\\\dot{\phi}\end{bmatrix} = \frac{1}{\cos\theta}\begin{bmatrix} 0 & \sin\phi & \cos\phi \\ 0 & \cos\theta\cos\phi & -\cos\theta\sin\phi \\ \cos\theta & \sin\theta\sin\phi & \sin\theta\cos\phi \end{bmatrix}\boldsymbol{\omega}^{\mathrm{b}}_{\mathrm{a,b}} \tag{2.11} $$

The differential kinematic equations for the Euler angles can then be solved as per Eq. (2.11). Note that there is a singularity in the Euler angle differential kinematics at $\theta = \pm 90^{\circ}$.

2.5 Nonlinear Kalman filtering

For theoretical understanding of the concept of the filters refer to Section 3.3. Only the mathematical description of the algorithm is provided below.

Consider a system/process and sensor/measurement model of the form where $\mathbf{x}$ is the state, $\mathbf{u}_p$ the process input, $\mathbf{u}_m$ the measurement input, $\mathbf{n}_p$ the process noise and $\mathbf{n}_m$ the measurement noise.

Process equation,

$$\mathbf{x}[k+1] = \mathbf{f}(\mathbf{x}[k], \mathbf{u}_p[k], \mathbf{n}_p[k]) \tag{2.12}$$

Measurement equation,

$$\mathbf{y}[k] = \mathbf{h}(\mathbf{x}[k], \mathbf{u}_m[k], \mathbf{n}_m[k]) \tag{2.13}$$

2.5.1 Extended Kalman Filter

The algorithm for state estimation via the EKF is given below (Wan and Van Der Merwe, 2001).

Initialization of state and covariance,

$$\begin{aligned} \hat{\mathbf{x}}[0] &= \mathbb{E}(\mathbf{x}[0]) \\ \mathbf{P}_{\mathbf{x}}[0] &= \mathbb{E}((\mathbf{x}[0] - \hat{\mathbf{x}}[0])(\mathbf{x}[0] - \hat{\mathbf{x}}[0])^{\mathrm{T}}) \end{aligned} \tag{2.14}$$

Predict step (*a prioiri estimates*),

$$\begin{aligned} \hat{\mathbf{x}}^{-}[k] &= \mathbf{f}(\hat{\mathbf{x}}[k-1], \mathbf{u}_p[k-1], \bar{\mathbf{n}}_p) \\ \mathbf{P}_{\mathbf{x}}^{-}[k] &= \mathbf{F}[k-1]\mathbf{P}_{\mathbf{x}}[k-1]\mathbf{F}^{\mathrm{T}}[k-1] + \mathbf{L}[k]\mathbf{Q}[k]\mathbf{L}^{\mathrm{T}}[k] \end{aligned} \tag{2.15}$$

Correct step (*a posteriori estimates*),

$$\begin{aligned} \mathbf{K}[k] &= \mathbf{P}_{\mathbf{x}}^{-}[k]\mathbf{H}^{\mathrm{T}}[k](\mathbf{H}[k]\mathbf{P}_{\mathbf{x}}^{-}[k]\mathbf{H}^{\mathrm{T}}[k] + \mathbf{M}[k]\mathbf{R}[k]\mathbf{M}^{\mathrm{T}}[k])^{-1} \\ \hat{\mathbf{x}}[k] &= \hat{\mathbf{x}}^{-}[k] + \mathbf{K}[k](\mathbf{y}[k] - \mathbf{h}(\hat{\mathbf{x}}^{-}[k], \mathbf{u}_m, \bar{\mathbf{n}}_m)) \\ \mathbf{P}_{\mathbf{x}}[k] &= (\mathbf{I} - \mathbf{K}[k]\mathbf{H}[k])\mathbf{P}_{\mathbf{x}}^{-}[k] \end{aligned} \tag{2.16}$$

Here $\mathbb{E}(\bullet)$ represents the expected value of $(\bullet)$ and $\bar{\mathbf{n}}_\bullet$ is $\mathbb{E}(\mathbf{n}_\bullet)$ which is equal to zero for Gaussian noise. $\mathbf{F}, \mathbf{L}, \mathbf{H}, \mathbf{M}$ are Jacobians given by Eq. (2.17).

$$
\begin{aligned}
\mathbf{F}[k] &= \frac{\partial \mathbf{f}(\mathbf{x}, \mathbf{u}_p[k], \bar{\mathbf{n}}_p)}{\partial \mathbf{x}}\Big|_{\hat{\mathbf{x}}_k} \\
\mathbf{L}[k] &= \frac{\partial \mathbf{f}(\hat{\mathbf{x}}^-[k], \mathbf{u}_p[k], \mathbf{n}_p)}{\partial \mathbf{n}_p}\Big|_{\bar{\mathbf{n}}_p} \\
\mathbf{H}[k] &= \frac{\partial \mathbf{h}(\mathbf{x}, \mathbf{u}_m[k], \bar{\mathbf{n}}_m)}{\partial \mathbf{x}}\Big|_{\hat{\mathbf{x}}[k]} \\
\mathbf{M}[k] &= \frac{\partial \mathbf{h}(\hat{\mathbf{x}}^-[k], \mathbf{u}_m[k], \mathbf{n}_m)}{\partial \mathbf{n}_m}\Big|_{\bar{\mathbf{n}}_m}
\end{aligned} \tag{2.17}
$$

2.5.2 Unscented Kalman Filter

The algorithm for state estimation via the UKF is given below (Wan and Van Der Merwe, 2001).

State and covariance is intialized same as Eq. (2.14). An augmented state and covariance matrix is used to generate the sigma points in a *non-additive noise* model as follows,

$$
\begin{aligned}
\hat{\mathbf{x}}^a[0] &= \mathbb{E}[\mathbf{x}^a[0]] = \begin{bmatrix}\hat{\mathbf{x}}^{\mathrm{T}}[0] & \mathbf{0} & \mathbf{0}\end{bmatrix}^{\mathrm{T}} \\
\mathbf{P}^a[0] &= \mathbb{E}[(\mathbf{x}^a[0] - \hat{\mathbf{x}}^a[0])(\mathbf{x}^a[0] - \hat{\mathbf{x}}^a[0])^{\mathrm{T}}] = \begin{bmatrix}\mathbf{P}[0] & \mathbf{0} & \mathbf{0} \\ \mathbf{0} & \mathbf{Q} & \mathbf{0} \\ \mathbf{0} & \mathbf{0} & \mathbf{R}\end{bmatrix} \\
\boldsymbol{\chi}^a[k-1] &= [\hat{\mathbf{x}}^a[k-1],\ \ \hat{\mathbf{x}}^a[k-1] + \gamma\sqrt{\mathbf{P}^a[k-1]},\ \ \hat{\mathbf{x}}^a[k-1] - \gamma\sqrt{\mathbf{P}^a[k-1]}]
\end{aligned} \tag{2.18}
$$

Predict step,

$$
\begin{aligned}
\boldsymbol{\chi}^x[k|k-1] &= \mathbf{f}(\boldsymbol{\chi}^{\mathbf{x}}[k-1], \mathbf{u}_p[k-1], \boldsymbol{\chi}^{\mathbf{n}_p}[k-1]) \\
\hat{\mathbf{x}}^-[k] &= \sum_{i=0}^{2L} W_i^{(m)} \boldsymbol{\chi}_i^{\mathbf{x}}[k|k-1] \\
\mathbf{P}^-[k] &= \sum_{i=0}^{2L} W_i^{(c)} (\boldsymbol{\chi}_i^{\mathbf{x}}[k|k-1] - \hat{\mathbf{x}}^-[k])(\boldsymbol{\chi}_i^{\mathbf{x}}[k|k-1] - \hat{\mathbf{x}}^-[k])^{\mathrm{T}} \\
\boldsymbol{\mathcal{Y}}_{k|k-1} &= \mathbf{h}(\boldsymbol{\chi}^{\mathbf{x}}[k|k-1], \boldsymbol{\chi}^{\mathbf{n}_m}[k-1]) \\
\hat{\mathbf{y}}^-[k] &= \sum_{i=0}^{2L} W_i^{(m)} \boldsymbol{\mathcal{Y}}_i[k|k-1]
\end{aligned} \tag{2.19}
$$

Correct step,

$$\begin{aligned}
\mathbf{P}_{\mathbf{yy}}[k] &= \sum_{i=0}^{2L} W_i^{(c)} (\boldsymbol{\mathcal{Y}}_i[k|k-1] - \hat{\mathbf{y}}^-[k])(\boldsymbol{\mathcal{Y}}_i[k|k-1] - \hat{\mathbf{y}}^-[k]) \\
\mathbf{P}_{\mathbf{xy}}[k] &= \sum_{i=0}^{2L} W_i^{(c)} (\boldsymbol{\chi}_i[k|k-1] - \hat{\mathbf{x}}^-[k])(\boldsymbol{\mathcal{Y}}_i[k|k-1] - \hat{\mathbf{y}}^-[k])^{\mathrm{T}} \\
\boldsymbol{\mathcal{K}}[k] &= \mathbf{P}_{\mathbf{xy}}[k]\mathbf{P}_{\mathbf{yy}}^{-1}[k] \\
\hat{\mathbf{x}}[k] &= \hat{\mathbf{x}}^-[k] + \boldsymbol{\mathcal{K}}[k][\mathbf{y}[k] - \hat{\mathbf{y}}^-[k] \\
\mathbf{P}_{\mathbf{x}}[k] &= \mathbf{P}^-[k] - \boldsymbol{\mathcal{K}}[k]\mathbf{P}_{\mathbf{yy}}[k]\boldsymbol{\mathcal{K}}^{\mathrm{T}}[k]
\end{aligned} \tag{2.20}$$

where

$$\begin{aligned}
\mathbf{x}^a &= [\mathbf{x}^{\mathrm{T}} \;\; \mathbf{n}_p^{\mathrm{T}} \;\; \mathbf{n}_m^{\mathrm{T}}]^{\mathrm{T}} \\
\boldsymbol{\chi}^a &= [(\boldsymbol{\chi}^{\mathbf{x}})^{\mathrm{T}} \;\; (\boldsymbol{\chi}^{\mathbf{n}_p})^{\mathrm{T}} \;\; (\boldsymbol{\chi}^{\mathbf{n}_m})^{\mathrm{T}}] \\
\gamma &= \sqrt{L + \lambda} \\
W_0^{(m)} &= \frac{\lambda}{L + \lambda} \\
W_0^{(c)} &= \frac{\lambda}{L + \lambda} + 1 - \alpha^2 + \beta \\
W_i^{(m)} &= W_i^{(c)} = \frac{1}{2(L + \lambda)} \\
\lambda &= \alpha^2(L + \kappa) - L
\end{aligned}$$

L is the dimension of the augmented state, κ is a secondary scaling parameter normally set to $L - 3$, α determines the spread of the points which is normally set to a small value like 10^{-4}, β is used to determine the type of distribution, for gaussian distributions $\beta = 2$ is optimal.

Chapter 3

State of the Art

This chapter reviews relevant literature to help put the development of topics addressed in this thesis into context. The state of the art covers the following topics:

- differential kinematic modelling of rovers
- terrain traversability and wheel-terrain contact angle
- estimation of states using nonlinear Kalman filters

3.1 Rover differential kinematics

The kinematic modelling of rovers is most often done using the Denavit-Hartenberg (DH) convention because of its simplicity (refer Section 2.2). In (Muir and Neuman, 1987) however the kinematic modelling of the rover is done using the Sheth-Uicker convention. The Sheth-Uicker convention has the advantage that it can be used to model links with multiple joints, in this case, an omnidirectional rolling wheel having 3 DOFs (2 translational and 1 rotational). This cannot be captured by the DH convention easily. Since the ExoMars rover does not have omnidirectional wheels, a regular approach to the kinematic modelling with the use of DH parameters is adopted.

In (Tarokh and McDermott, 2007) a generalization of the kinematic modelling for modern rovers using the DH parameters is proposed. They start with the basic velocity propagation equations for robotic links and derive them in terms of the DH parameters. They arrive at the equations relating velocity and rotation rates in the rover reference frame (denoted by g) to those in the wheel contact frame (denoted by c) as shown in Eq. (3.1)

$$\begin{bmatrix} \mathbf{v}^{\mathrm{g}}_{\mathrm{i,g}} \\ \boldsymbol{\omega}^{\mathrm{g}}_{\mathrm{i,g}} \end{bmatrix} = \mathbf{E}_{\mathrm{n}} \begin{bmatrix} \mathbf{v}^{\mathrm{c}}_{\mathrm{i,c_n}} \\ \boldsymbol{\omega}^{\mathrm{c}}_{\mathrm{i,c_n}} \end{bmatrix} + \mathbf{F}_{\mathrm{n}} \dot{\mathbf{P}}_{\mathrm{n}} \tag{3.1}$$

Here the index n refers to the n^{th} wheel, $\mathbf{E}, \mathbf{F}$ are matrices that are solely dependent on the DH parameters, $\dot{\mathbf{P}}$ is the matrix containing the derivatives of the DH parameters. The approach used in this thesis is equivalent to the one described above.

Recently, in (Toupet et al., 2018) the modelling of the kinematics of the rover is done not with the use of DH parameters, but with a simple systematic follow-through of link velocities. This is done in an intuitive manner by taking the rotation rates and lever arms concerned with the various links to arrive at the kinematics relating velocity in reference frame to that in wheel frame. Although this approach is manageable for a simple rover system with not too many links, it offers no significant advantage over the standardized DH parameters.

3.2 Terrain traversability & wheel-terrain contact angle

3.2.1 Terrain traversability

The motivation behind studying the wheel-terrain interaction is to in some way predict the traversability of the terrain. A lot of research has been dedicated to studying the mechanics of interaction between the wheels and terrain. This branch of study is broadly termed *terramechanics*. In this domain determining terrain traversability is done mostly via the study of wheel-terrain contact forces (Ray, 2009) and the soil mechanical parameters like cohesion and friction (Iagnemma et al., 2004; Hutangkabodee et al., 2006; Li et al., 2018).

Aside from terrain parameter and force estimation, traversability can also be studied from the inertial navigation system. The inertial navigation system determines the acceleration and rotation of the vehicle commonly with the use of onboard accelerometers and gyroscopes. Normally the measurements from the accelerometer and gyroscope are very noisy and unreliable especially for slow speed rovers. Therefore to purely rely on the IMU for the velocity and orientation is not a good choice. In (Stavens and Thrun, 2012) the terrain roughness is estimated for autonomous driving of off-road vehicles from the inertial navigation system. Here a machine learning algorithm is implemented for determining the second derivative of the ground to characterize the terrain roughness by training the lasers used for visual odometry with shock data from accelerometers. This approach requires

large onboard computing capabilities and additional sensors like cameras which are expensive.

3.2.2 Wheel-terrain contact angle

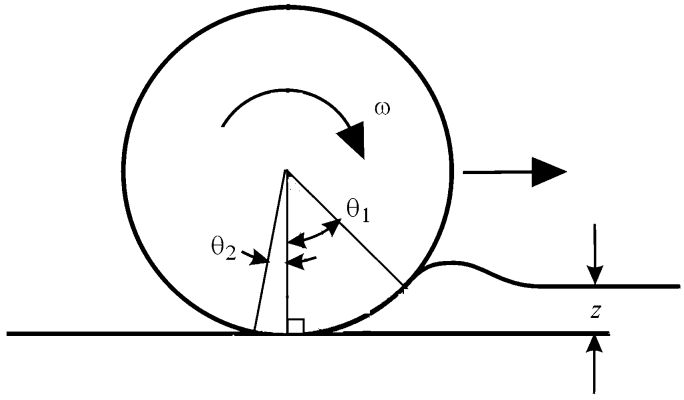

Figure 3.1: Entrance (θ_1) and exit (θ_2) angle of a wheel in relation to sinkage z. Image adapted from (Iagnemma et al., 2004) Copyright ©2004, IEEE.

Studies related to wheel-terrain contact in the field of terramechanics mainly includes the study of stresses and forces developed at the wheel-terrain contact patch. In this context the *contact angle* (Junlong et al., 2017; Reina et al., 2008; Li et al., 2018) or *contact region* (Doumiati et al., 2008) or *contact arc* (Cross et al., 2013) refers to the angle formed by the arc between the point of exit and entry of the wheel in the soil (refer Fig. 3.1). The shear stresses and normal pressure distribution across the contact region, when integrated between the entry and exit angles of the wheel, give the resistance force and torques developed at the wheel-terrain interface. The estimation of resistance force and torques are useful in the computation of the wheel motor power needed to overcome them. A contact model that predicts the contact forces and reaction torques has been developed with the estimation of entry and exit angles in (Leite et al., 2012). However here the mechanical properties of the soil, namely, friction angle and cohesion which are parameters needed for the estimation, have been assumed to be known *a priori*, which is not the case for planetary exploration terrain. The entrance and exit angles have been calculated in (Li et al., 2018) from measured values of wheel sinkage. The wheel sinkage is related to the entrance and exit angle by $z = r_{\mathrm{w}}(1 - \cos\theta)$ where z is the wheel sinkage at the entrance or exit, r_{w} the wheel radius, θ the corresponding

entrance or exit angle. These angles are then used to calculate the reaction forces and torques. A visual method has been used to determine similar contact angles to compute the wheel sinkage (Reina et al., 2008) as a characterization of mobility on the concerned terrain. Similarly, specially designed wheels equipped with magnetic angular sensors (Junlong et al., 2017) have been employed to measure contact angles and then calculate the wheel sinkage. These are a few examples of studies on contact angle as referred to in the context of terramechanics.

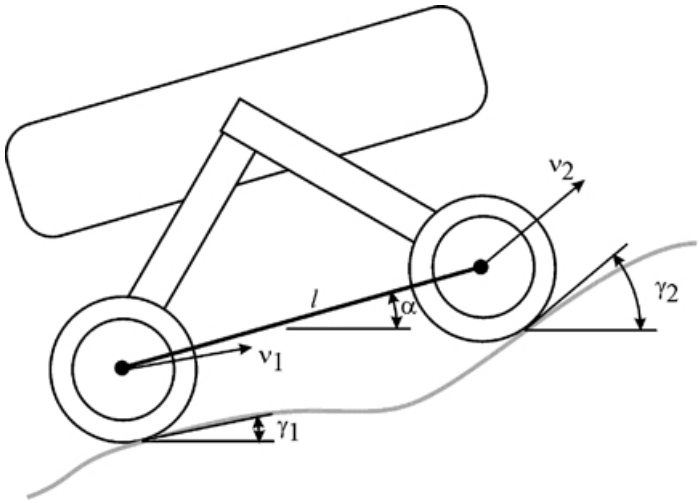

Figure 3.2: Contact angles as defined by from a kinematic perspective. Image taken from reprint in (Iagnemma et al., 2003) Copyright ©2003, Kluwer Academic Publications

It is important to make the distinction in the terminology of contact angle in the exiting literature and therefore for the sake of completeness this perspective of contact angle was described above. However this thesis does *not* deal with the contact angle in the context of entrance and exit points of wheel-terrain contact. The contact angle, as addressed in this thesis, is an indicator of terrain unevenness. In this context the wheel-ground contact angles have been estimated using onboard sensors to improve traction and reduce motor power consumption (Iagnemma and Dubowsky, 2000b). The wheel-ground contact angles influence how the vehicle applies force on the ground (Iagnemma et al., 2001). The contact angle estimates are used in the development of actively articulated suspensions for rovers to improve stability in (Iagnemma et al., 2003). Here it is stated that, *'an "effective" wheel-terrain contact angle is defined as the angular direction of travel imposed on the wheel by the terrain during motion'*. An analytical solution to the contact angles is derived from the kinematics of the rover which is reproduced in Eq. (3.3). Fig. 3.2 shows the schematic used to develop the kinematics. The constraint ap-

plied to the kinematics is a geometric constraint where the distance between the wheels attached to a bogie cannot change and therefore equating the components of velocity in the direction of the link connecting the wheels in Eq. (3.2) gives the solution for contact angles as in Eq. (3.3).

$$\begin{aligned} v_1 \cos(\gamma_1 - \alpha) &= v_2 \cos(\gamma_2 - \alpha) \\ v_2 \sin(\gamma_2 - \alpha) - v_1 \cos(\gamma_1 - \alpha) &= l\dot{\alpha} \end{aligned} \tag{3.2}$$

v_1, v_2 are the respective wheel velocities, γ_1, γ_2 the respective contact angles, α the pitch angle, and l the distance between wheels attached to a bogie. Solving Eq. (3.2) analytically, the contact angles are

$$\begin{aligned} \gamma_1 &= \alpha - \cos^{-1}(h) \\ \gamma_2 &= \cos^{-1}(h/b) + \alpha \end{aligned} \tag{3.3}$$

where,

$$h = \frac{1}{2a}\sqrt{2a^2 + 2b^2 + 2a^2b^2 - a^4 - b^4 - 1};\ a = \frac{l\dot{\alpha}}{v_1};\ b = \frac{v_2}{v_1}$$

Iagnemma et al. model the contact angle state as a *random walk* i.e. its rate of change is equal to random noise. The reasoning for this being that it is not known how the contact angles will evolve over time without the knowledge of the terrain. This approach is also adopted in this thesis. Iagnemma et al. also assume that the wheel velocities can be approximated using the wheel turn rates and wheel radii. This means that wheel slip is ignored in the estimation, which is not a good assumption for all terrains, for example sandy loose soils. This thesis will address the estimation of contact angles along with wheel slip.

In (Balaram, 2000) a *damped model* is considered in modelling the dynamic state of contact angle. The assumption made is that the terrain has a moderate curvature. The damped model brings the contact angle back to a steady-state which is desirable for a smooth terrain. Additionally it is assumed that the contact points on wheels attached to the same bogie are symmetrical and can be modelled with a single contact state. This approximation however will not hold true for a rough terrain. In this thesis the contact angle of each individual wheel is taken to be independent of the others.

Contact angles, defined similar to (Iagnemma and Dubowsky, 2000a), are calculated with an input reference rover velocity mapped down to wheel velocities using rover orientation and joint angle measurements in (Peynot and Lacroix, 2003).

The velocities of wheels derived from the wheel rate measurements are then compared with those obtained from the previously calculated contact angles for wheels attached to a rigid link. There will be discrepancies if any of the wheels experience slip and these discrepancies are a measure of what they term *speed coherence indicators*. These speed coherence indicators are then fed into a complex algorithm combining *supervised learning* results and probabilistic determination of rover state, to minimize slippage of rover on rough terrain. In this paper the approximate contact angle is calculated as an ad hoc parameter that is used as an input to an algorithm that then monitors the locomotion with some indicators and adapts the motion control accordingly. In this thesis the primary focus is to estimate the actual contact angles with good accuracy along with an estimation of the rover velocity and wheel slips from measurements of onboard sensors. No reference velocities or desired turn rates will be used for the estimation.

In (Tarokh and McDermott, 2005) the contact angle is defined as the angle between the steering axis and the normal to the direction of wheel velocity (refer Fig. 3.3). The relation between the pose of the rover and the degrees of freedom vector is derived and the final equation is as per (Eq. (3.4)).

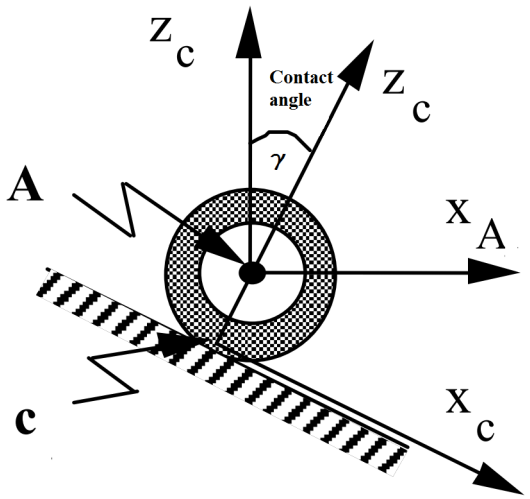

Figure 3.3: Contact angles as defined by Tarokh et al. Image adapted from (Tarokh and McDermott, 2007) Copyright ©2005, IEEE. **A** refers to the steering frame and **C** to the contact frame.

$$\begin{bmatrix} \mathbf{I}_6 \\ \mathbf{I}_6 \\ \vdots \\ \mathbf{I}_6 \end{bmatrix} \begin{bmatrix} \mathbf{v}^{\mathrm{g}}_{\mathrm{i,g}} \\ \boldsymbol{\omega}^{\mathrm{g}}_{\mathrm{i,g}} \end{bmatrix} = \mathbf{J}(\mathbf{q})\dot{\mathbf{q}}$$

$$\mathbf{E}\mathbf{u} = \mathbf{J}(\mathbf{q})\dot{\mathbf{q}} \tag{3.4}$$

$\mathbf{v}^{\mathrm{g}}_{\mathrm{i,g}}$ is the rover velocity, $\boldsymbol{\omega}^{\mathrm{g}}_{\mathrm{i,g}}$ the rotation rates of the rover and $\mathbf{q}$ the vector containing all the joint angles, wheel rates, **contact angles**, turn slip, roll slip and side slip for all wheels. $\mathbf{J}$ is the kinematic Jacobian relating the rover linear and rotational velocities to the degrees of freedom vector. $\mathbf{E}$ is a matrix of stacked identity matrices equal to the number of wheels and $\mathbf{u}$ is the pose of the rover. The measured and non-measured parameters are seperated out from Eq. (3.4) as in Eq. (3.5). The subscripts m and nm refer to measurable and non-measurable quantities respectively.

$$\begin{bmatrix} \mathbf{E}_m & \mathbf{E}_{nm} \end{bmatrix} \begin{bmatrix} \mathbf{u}_m \\ \mathbf{u}_{nm} \end{bmatrix} = \begin{bmatrix} \mathbf{J}_m(\mathbf{q}) & \mathbf{J}_{nm}(\mathbf{q}) \end{bmatrix} \begin{bmatrix} \dot{\mathbf{q}}_m \\ \dot{\mathbf{q}}_{nm} \end{bmatrix} \tag{3.5}$$

Eq. (3.5) can be rearranged as in Eq. (3.6) and then a weighted least squares method is applied to solve for unknown quantities. The velocity vector, yaw rate, slip rate and **contact angle rates** are taken as non-measured quantities and the roll rate, pitch rate, joint angles and wheel rates are taken as measured quantities. $\mathbf{W}$ is a weighting matrix.

$$\begin{bmatrix} \mathbf{E}_{nm} & -\mathbf{J}_{nm}(\mathbf{q}) \end{bmatrix} \begin{bmatrix} \mathbf{u}_{nm} \\ \dot{\mathbf{q}}_{nm} \end{bmatrix} = \begin{bmatrix} -\mathbf{E}_m & \mathbf{J}_m(\mathbf{q}) \end{bmatrix} . \begin{bmatrix} \mathbf{u}_m \\ \dot{\mathbf{q}}_m \end{bmatrix}$$

$$\mathbf{A}\mathbf{X} = \mathbf{B}\mathbf{Y}$$

$$\mathbf{X} = (\mathbf{A}^{\mathrm{T}}\mathbf{W}\mathbf{A})^{-1}\mathbf{A}^{\mathrm{T}}\mathbf{W}\mathbf{B}\mathbf{Y} \tag{3.6}$$

This approach is however validated with an elevation map from a known terrain in the simulation and therefore does not truly address the estimation of unknown contact angles. Although the quantities are separated into measured and non-measured quantities, they cannot be seperated out from the Jacobians which depend on the entire vector $\mathbf{q}$ which contains the unknown contact angle.

Recently in (Toupet et al., 2018), the contact angle, which is defined as in (Tarokh and McDermott, 2005), has been estimated. An equivalent definition of contact angle is adopted in this thesis (introduced in Section 5.1). The objective in (Toupet

et al., 2018) is to calculate the ideal zero-slip wheel rates for which the contact angle is required to be estimated first. In order to estimate the contact angle an initial assumption made is that the rover velocity can be approximated to that on smooth ground i.e lateral and vertical velocities set to zero. The requirement is to operate the rover at maximum speed and to calculate the ideal wheel speeds with the knowledge of contact angles. An approximation for the rover velocity is made for straight-driving conditions. The wheel velocity is then calculated from the kinematics using the suspension angles and rates as measurements. The contact angle is then computed as the angle between the components of the wheel velocity in the wheel plane. In order to compute the ideal wheel rates, now a *reverse calculation* of rover velocity is done by first setting all wheels to maximum wheel rate and incorporating the previously computed contact angles. The lateral rover velocity component is assumed zero to negate any sideways motion. The rover velocity computed from each wheel will be different when any of the wheels have unequal non-zero contact angles. The wheel that leads to the minimum absolute rover velocity, taken as a limiting value, is then set to the maximum wheel rate and the ideal wheel rates for the remaining wheels calculated from the kinematics. This paper shows a simple application of contact angle however the focus is not on estimating them accurately and therefore several assumptions are made. In this thesis for the *contact angle model* a similar assumption of ignoring lateral wheel velocities is made. However the *contact & side slip angle model* takes into account both vertical and lateral wheel velocities in the estimation of contact angles.

3.3 Estimation

Several estimation techniques exist like the maximum likelihood, least squares and the Kalman filter, to name a few (Saridis, 1983). In (Tarokh and McDermott, 2005) a weighted least squares approach is used to estimate the unknowns (including contact angle rates) and an analysis of the existence of solutions is done based on the ranks of the matrices. The focus in this thesis is on nonlinear Kalman filters and therefore the discussion ahead is restricted to these. The Kalman filter, credited to R E Kalman (Kalman, 1960), is a recursive algorithm which is used to find the optimal estimate of the state of the system by minimizing the mean of the square error (Welch and Bishop, 2006). The current state of the system is propagated through the linear process/state equation to generate the *a priori* mean and covariance of the states in the predict step (refer Section 2.5.1 for complete algorithm). The predicted states are propagated through the linear measurement equation to generate the predicted measurement. The error between the predicted and actual measurement is then compensated for in the *a posteriori* state with a weighting of the error that determines how much the filter trusts the *a priori* state

against the innovation term. The weighting term is called the Kalman gain. The Kalman filter is however only applicable to linear systems. The algorithm can work in real-time and it only requires the estimate of the previous state and current inputs (Wan and Van Der Merwe, 2001). For nonlinear systems, most commonly the extended Kalman filter (EKF) or unscented Kalman filter (UKF) are used to find the best estimates.

The EKF is an extension of the Kalman filter to handle nonlinear systems (Maybeck, 1979). Here the Kalman gain is computed from the Jacobians using first-order linearization of the state transition and measurement matrices. The algorithm for non-additive process and measurement noise EKF taken from (Wan and Van Der Merwe, 2001) is given in Section 2.5.1 . The UKF was proposed by Julier and Uhlmann to tackle highly nonlinear systems where the first-order linearization used in EKF resulted in highly inconsistent and sometimes divergent estimates (Julier and Uhlmann, 1997). The UKF does not require the computation of state transition and measurement Jacobians and its accuracy is at par with a second-order linearisation of the nonlinear system. The algorithm generates a number of sample points from a gaussian distribution called sigma points with the mean and covariance of the current state. These sigma points are then propagated through the nonlinear state equation which generates a number of predicted states. A gaussian distribution is fit to these predicted states and the new mean and covariance computed. Similarly sigma points are generated and propagated through the measurement equation. The Kalman gain is computed with the covariances of the states and measurements and the innovation term is weighted to get the corrected state. The algorithm for non-additive process and measurement noise UKF taken from (Wan and Van Der Merwe, 2001) is given in Section 2.5.2.

In (Iagnemma and Dubowsky, 2000a) for the estimation of contact angles modelled as a random walk, an EKF is implemented and the possibility of a UKF is suggested. As mentioned before in Section 3.2.2 since the wheel velocities which are needed for computing the contact angles, are approximated from wheel rates and radii, the slip is ignored in the EKF implementation.

Balram implements the contact angle as a damped model and uses an EKF for the estimation of rover velocity (Balaram, 2000). The wheel slip is related to the forward kinematics of the rover for each wheel. In the extended Kalman filter implementation, a *deterministic* value of slip for smooth terrain is calculated and used as a *measurement* in the filter. The rotation slip of the wheel is approximated with a deterministic value computed from the turn rate and steering angles, and the transversal slip induced during turns is similarly computed for non-steered wheels.

In this thesis the wheel slip is not approximated, instead, it is estimated along with the rover velocity and contact angles.

To summarize, this thesis develops on ideas inspired by the approaches reviewed above in the area of differential kinematic modelling of the rover, definition and modelling of wheel-terrain contact angle and estimation of contact angle using nonlinear Kalman filters. As previously stated, the existing framework at DLR only estimates the rover velocity and wheel slip for smooth terrain drive. The following chapter details the kinematics and filter implementation for this existing framework, upon which the following work in this thesis is built.

Chapter 4

Velocity and slip estimator for smooth terrain

This chapter describes the existing framework for the estimation of rover velocity and wheel slip. The idea is to first develop the kinematic relations between the rover velocity and the individual wheel velocities. In this thesis it shall be referred to as the wheel Jacobian, which is a Jacobian relating the wheel velocity to the joint rates of the rover, the rover velocity and its orientation. Then the kinematic equations of motion describing the states of the system that are of interest are developed. Upon establishing the kinematic model of the whole system, measurements from various sensors (IMU, potentiometers, wheel encoders) are fused using a filter to estimate the rover velocity and wheel slip. The system, once modelled, is a nonlinear one and therefore a nonlinear filter is proposed for state estimation, in this case, the extended or unscented Kalman filter.

The existing framework for rover velocity and wheel slip estimation was developed under the condition that the rover travels on smooth terrain and the lateral and vertical wheel velocities are assumed to be zero. Section 4.1 first defines the wheel slip, Section 4.2 derives the *wheel Jacobian*. Following this, in Section 4.3 the kinematic equations of motion used to develop the state equations for the nonlinear Kalman filter are explained. Section 4.4 describes the set-up of the process and measurement models for the nonlinear Kalman filter and in Section 4.5 the parameter settings for the filter implementation are discussed. Section 4.6 briefly comments on a limitation of the measurement equation used in the filter.

4.1 Longitudinal wheel slip

The longitudinal wheel slip is defined as the ratio of slip speed to pure rolling speed along the wheel rolling plane

$$s = \frac{\omega_{\mathrm{w}} r_{\mathrm{w}} - v_x}{\omega_{\mathrm{w}} r_{\mathrm{w}}} = 1 - \frac{v_x}{\omega_{\mathrm{w}} r_{\mathrm{w}}} \tag{4.1}$$

where ω_{w}, and r_{w} are the measurable rotational wheel speed and known wheel radius and v_x is the **longitudinal** component of wheel velocity in the wheel frame considered. The interpretation of the slip values is summarized below

$s < 0$: wheel moves faster than its rolling speed

$s = 0$: pure rolling motion

$0 < s < 1$: wheel moves slower than its rolling speed

$s = 1$: pure slip when wheel is in rotation without translation

$s > 1$: wheel moves opposite to the direction of rolling velocity

The longitudinal slip definition has a **singularity** when the wheel rate is zero.

4.2 Wheel Jacobian

Table 4.1 and Fig. 4.1 show the frames and notations used to develop the kinematics. Note that the frames are assigned such that they are fixed to the concerned joint but do not rotate with the corresponding link, rather with the preceding link. For example, the steering frame does not rotate with the steering link but with the preceding link i.e. the bogie. Also note that the link between the body frame containing the CoG frame and the bogie frame has no degree of freedom, therefore it is a fixed link.

Table 4.1: Notations used. Note -$\mathrm{a}, \mathrm{b}, \mathrm{c}$ refer to frames

Notation	Description
$\mathbf{r}^{\mathrm{c}}_{\mathrm{a,b}}$	Position vector from origin of a to b expressed in c
$\mathbf{v}^{\mathrm{c}}_{\mathrm{a,b}}$	Velocity of b with respect to a expressed in c
$\boldsymbol{\omega}^{\mathrm{c}}_{\mathrm{a,b}}$	Angular velocity of b with respect to a expressed in c
$\mathbf{R}^{\mathrm{b}}_{\mathrm{a}}$	Rotation matrix transforming a to b
q_{b}	Bogie rotation
q_{s}	Steering rotation

The wheel Jacobian for a single wheel is first derived under the assumption that the rover is travelling on a *smooth terrain* with **zero lateral** and **vertical** wheel velocity components. Refer to Section 2.1 for basics of coordinate transformations. Fig. 4.2 shows a schematic representation of the frames in vector space which can be used to easily derive the kinematics of the rover.

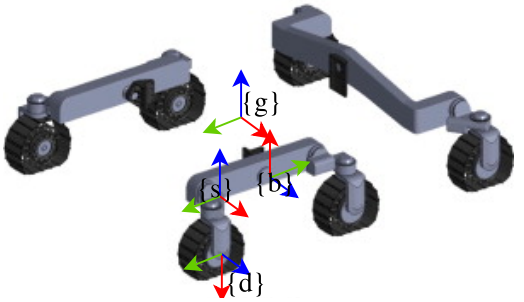

Frame	Description
i	Inertial frame
g	Rover CoG frame
b	Bogie frame
s	Steering frame
d	Drive frame at wheel hub

Figure 4.1: Coordinate frames assigned to the ExoMars BB2 model. Green, red and blue depict the x,y and z axes respectively. Image adapted from (Patel et al., 2010) Copyright ©2010, ISTVS.

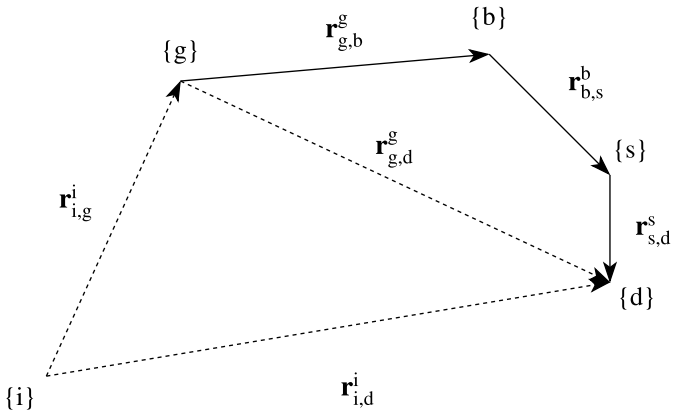

Figure 4.2: Coordinate frames in vector space

From Fig. 4.2

$$\mathbf{r}^{\mathrm{i}}_{\mathrm{i,d}} = \mathbf{r}^{\mathrm{i}}_{\mathrm{i,g}} + \mathbf{R}^{\mathrm{i}}_{\mathrm{g}}\mathbf{r}^{\mathrm{g}}_{\mathrm{g,d}} \tag{4.2}$$

By taking the derivative of Eq. (4.2) and transforming it to the drive frame

$$\mathbf{v}^{\mathrm{d}}_{\mathrm{i,d}} = \mathbf{R}^{\mathrm{d}}_{\mathrm{g}}\mathbf{v}^{\mathrm{g}}_{\mathrm{i,g}} + \mathbf{R}^{\mathrm{d}}_{\mathrm{g}}[\boldsymbol{\omega}^{\mathrm{g}}_{\mathrm{i,g}}\times]\mathbf{r}^{\mathrm{g}}_{\mathrm{g,d}} + \mathbf{R}^{\mathrm{d}}_{\mathrm{g}}\mathbf{v}^{\mathrm{g}}_{\mathrm{g,d}} \tag{4.3}$$

$\mathbf{v}^{\mathrm{g}}_{\mathrm{i,g}}$ is the rover velocity that is to be estimated along with wheel slip, $\boldsymbol{\omega}^{\mathrm{g}}_{\mathrm{i,g}}$ is the rotation rate of the rover taken from the IMU gyroscope measurements, $\mathbf{r}^{\mathrm{g}}_{\mathrm{g,d}}$ and $\mathbf{v}^{\mathrm{g}}_{\mathrm{g,d}}$ are derived from the kinematics of the rover as

$$\begin{aligned}\mathbf{r}^{\mathrm{g}}_{\mathrm{g,d}} &= \mathbf{r}^{\mathrm{g}}_{\mathrm{g,b}} + \mathbf{R}^{\mathrm{g}}_{\mathrm{b}}\mathbf{r}^{\mathrm{b}}_{\mathrm{b,s}} + \mathbf{R}^{\mathrm{g}}_{\mathrm{s}}\mathbf{r}^{\mathrm{s}}_{\mathrm{s,d}} \\ \mathbf{v}^{\mathrm{g}}_{\mathrm{g,d}} &= \mathbf{R}^{\mathrm{g}}_{\mathrm{b}}[\boldsymbol{\omega}^{\mathrm{b}}_{\mathrm{b,s}}\times]\mathbf{r}^{\mathrm{b}}_{\mathrm{b,s}} + \mathbf{R}^{\mathrm{g}}_{\mathrm{b}}\dot{\mathbf{r}}^{\mathrm{b}}_{\mathrm{b,s}} + \mathbf{R}^{\mathrm{g}}_{\mathrm{s}}[\boldsymbol{\omega}^{\mathrm{s}}_{\mathrm{b,s}}\times]\mathbf{r}^{\mathrm{s}}_{\mathrm{s,d}}\end{aligned} \tag{4.4}$$

$\mathbf{r}^{\mathrm{g}}_{\mathrm{g,b}}$ is constant since there is no degree of freedom between the CoG and bogie frame as stated earlier, and $\mathbf{r}^{\mathrm{s}}_{\mathrm{s,d}}$ is also constant since the rotation about the steering axis is aligned with the direction of $\mathbf{r}^{\mathrm{s}}_{\mathrm{s,d}}$, i.e the vector joining the origin of the two frames. However $\mathbf{r}^{\mathrm{b}}_{\mathrm{b,s}}$ is not constant since the steering frame rotates with respect to the bogie frame by the bogie angle q_{b} and $\dot{\mathbf{r}}^{\mathrm{b}}_{\mathrm{b,s}}$ is unknown. Alternatively Eq. (4.4) can be written as

$$\begin{aligned}\mathbf{r}^{\mathrm{g}}_{\mathrm{g,d}} &= \mathbf{r}^{\mathrm{g}}_{\mathrm{g,b}} + \mathbf{R}^{\mathrm{g}}_{\mathrm{s}}\mathbf{r}^{\mathrm{s}}_{\mathrm{b,s}} + \mathbf{R}^{\mathrm{g}}_{\mathrm{s}}\mathbf{r}^{\mathrm{s}}_{\mathrm{s,d}} \\ \mathbf{v}^{\mathrm{g}}_{\mathrm{g,d}} &= \mathbf{R}^{\mathrm{g}}_{\mathrm{s}}[\boldsymbol{\omega}^{\mathrm{s}}_{\mathrm{b,s}}\times](\mathbf{r}^{\mathrm{s}}_{\mathrm{b,s}} + \mathbf{r}^{\mathrm{s}}_{\mathrm{s,d}})\end{aligned} \tag{4.5}$$

$\mathbf{r}^{\mathrm{s}}_{\mathrm{b,s}}$ is constant since the steering frame is rotating with the bogie and therefore the vector pointing from the origin of steering frame to origin of bogie frame as seen from the steering frame is always a constant. Inserting Eq. (4.5) into Eq. (4.3)

$$\mathbf{v}^{\mathrm{d}}_{\mathrm{i,d}} = \mathbf{R}^{\mathrm{d}}_{\mathrm{g}}\Big(\mathbf{v}^{\mathrm{g}}_{\mathrm{i,g}} + [\boldsymbol{\omega}^{\mathrm{g}}_{\mathrm{i,g}}\times](\mathbf{r}^{\mathrm{g}}_{\mathrm{g,b}} + \mathbf{R}^{\mathrm{g}}_{\mathrm{s}}(\mathbf{r}^{\mathrm{s}}_{\mathrm{b,s}} + \mathbf{r}^{\mathrm{s}}_{\mathrm{s,d}})) + \mathbf{R}^{\mathrm{g}}_{\mathrm{s}}[\boldsymbol{\omega}^{\mathrm{s}}_{\mathrm{b,s}}\times](\mathbf{r}^{\mathrm{s}}_{\mathrm{b,s}} + \mathbf{r}^{\mathrm{s}}_{\mathrm{s,d}})\Big) \tag{4.6}$$

where,

$$\begin{aligned}\mathbf{R}^{\mathrm{d}}_{\mathrm{g}} &= \mathbf{R}^{\mathrm{d}}_{\mathrm{s}}(q_{\mathrm{s}})\mathbf{R}^{\mathrm{s}}_{\mathrm{b}}(q_{\mathrm{b}})\mathbf{R}^{\mathrm{b}}_{\mathrm{g}} \\ \mathbf{v}^{\mathrm{g}}_{\mathrm{i,g}} &= \begin{bmatrix}\dot{x} & \dot{y} & \dot{z}\end{bmatrix}^{\mathrm{T}} \\ \boldsymbol{\omega}^{\mathrm{s}}_{\mathrm{b,s}} &= \begin{bmatrix}0 & 0 & \dot{q_{\mathrm{b}}}\end{bmatrix}^{\mathrm{T}}\end{aligned}$$

(x, y, z) is the position of the rover in inertial space and $\boldsymbol{\omega}^{\mathrm{g}}_{\mathrm{i,g}}$ is the rover angular velocity vector measured by the IMU gyroscope. Eq. (4.6) is the traditional explicit deduction of motion of the end-effector and so far only a single wheel was considered. Instead of expanding the velocity and position of the wheel in the

drive frame with respect to the CoG frame as in Eq. (4.5), it is commonly derived in robotics from the DH transformation matrices (refer Section 2.2) and then the Jacobian matrix is computed (refer Section 2.3). Table 4.2 shows the DH parameters for the ExoMars rover. Eq. (4.6) is now replaced with the Jacobian derived from DH parameters and the formulation extended to all wheels of the rover.

Table 4.2: DH table for ExoMars BB2

Link	$\boldsymbol{\theta}_i$	$\mathbf{d}_i$	$\mathbf{a}_i$	$\boldsymbol{\alpha}_i$
$\mathrm{g} \rightarrow \mathrm{b_{FL}}$	π	0.1600	-0.3305	$\pi/2$
$\mathrm{g} \rightarrow \mathrm{b_{FR}}$	0	0.1600	0.3305	$\pi/2$
$\mathrm{g} \rightarrow \mathrm{b_{R}}$	$-\pi/2$	0.2300	0.0000	$\pi/2$
$\mathrm{b_{FL}} \rightarrow \mathrm{s_{FL}}$	$\pi + q_{\mathrm{b_{FL}}}$	0.5933	0.3200	$\pi/2$
$\mathrm{b_{FL}} \rightarrow \mathrm{s_{ML}}$	$\pi + q_{\mathrm{b_{FL}}}$	0.6013	-0.3200	$\pi/2$
$\mathrm{b_{R}} \rightarrow \mathrm{s_{RL}}$	$\pi + q_{\mathrm{b_{R}}}$	0.6980	0.6043	$\pi/2$
$\mathrm{b_{R}} \rightarrow \mathrm{s_{RR}}$	$\pi + q_{\mathrm{b_{R}}}$	0.6980	-0.5963	$\pi/2$
$\mathrm{b_{FR}} \rightarrow \mathrm{s_{MR}}$	$\pi + q_{\mathrm{b_{FR}}}$	0.5933	0.3200	$\pi/2$
$\mathrm{b_{FR}} \rightarrow \mathrm{s_{FR}}$	$\pi + q_{\mathrm{b_{FR}}}$	0.6013	-0.3200	$\pi/2$
$\mathrm{s_{FL}} \rightarrow \mathrm{d_{FL}}$	$q_{\mathrm{s_{FL}}}$	-0.2160	0.0000	$-\pi/2$
$\mathrm{s_{ML}} \rightarrow \mathrm{d_{ML}}$	$q_{\mathrm{s_{ML}}}$	-0.2160	0.0000	$-\pi/2$
$\mathrm{s_{RL}} \rightarrow \mathrm{d_{RL}}$	$-\pi/2 + q_{\mathrm{s_{RL}}}$	-0.2860	0.0000	$-\pi/2$
$\mathrm{s_{RR}} \rightarrow \mathrm{d_{RR}}$	$-\pi/2 + q_{\mathrm{s_{RR}}}$	-0.2860	0.0000	$-\pi/2$
$\mathrm{s_{MR}} \rightarrow \mathrm{d_{MR}}$	$\pi + q_{\mathrm{s_{MR}}}$	-0.2160	0.0000	$-\pi/2$
$\mathrm{s_{FR}} \rightarrow \mathrm{d_{FR}}$	$\pi + q_{\mathrm{s_{FR}}}$	-0.2160	0.0000	$-\pi/2$

FL : Front Left; FR : Front Right; R : Rear;
ML : Middle Left; MR : Middle Right;
RL : Rear Left; RR : Rear Right

The transformation matrix for the n^{th} wheel derived from the DH parameters is

$$\mathbf{T}^{\mathrm{g}}_{\mathrm{d_n}} = \begin{bmatrix} \mathbf{R}^{\mathrm{g}}_{\mathrm{d_n}} & \mathbf{r}^{\mathrm{g}}_{\mathrm{g,d_n}} \\ \mathbf{0} & 1 \end{bmatrix}$$

$$\mathbf{v}^{\mathrm{g}}_{\mathrm{g,d_n}} = \frac{\partial \mathbf{r}^{\mathrm{g}}_{\mathrm{g,d_n}}}{\partial \mathbf{q}}\, \dot{\mathbf{q}} = \mathbf{J}_{\mathrm{n}}\, \dot{\mathbf{q}} \tag{4.7}$$

The subscript $\mathrm{n} \in \{\mathrm{FL}, \mathrm{ML}, \mathrm{RL}, \mathrm{RR}, \mathrm{MR}, \mathrm{FR}\}$ is used to index the drive and steering frames associated with the respective wheels. $\mathbf{q}$ is the full vector comprised of all the bogie and steering angles.

$$\mathbf{q} = \begin{bmatrix} q_{\mathrm{b_{FL}}} & q_{\mathrm{b_{FR}}} & q_{\mathrm{b_{R}}} & q_{\mathrm{s_{FL}}} & q_{\mathrm{s_{ML}}} & q_{\mathrm{s_{RL}}} & q_{\mathrm{s_{RR}}} & q_{\mathrm{s_{MR}}} & q_{\mathrm{s_{FR}}} \end{bmatrix}^{\mathrm{T}}$$

Substituting for $\mathbf{r}^{\mathrm{g}}_{\mathrm{g,d}}$ and $\mathbf{v}^{\mathrm{g}}_{\mathrm{g,d}}$ from Eq. (4.7) into Eq. (4.3) and rewriting in the Jacobian form

$$\mathbf{v}^{\mathrm{d_n}}_{\mathrm{i,d_n}} = \underbrace{\begin{bmatrix} {}^{v}\mathbf{J}_{\mathrm{n}} & {}^{\omega}\mathbf{J}_{\mathrm{n}} & {}^{q}\mathbf{J}_{\mathrm{n}} \end{bmatrix}}_{wheel\ Jacobian} \begin{bmatrix} \mathbf{v}^{\mathrm{g}}_{\mathrm{i,g}} \\ \boldsymbol{\omega}^{\mathrm{g}}_{\mathrm{i,g}} \\ \dot{\mathbf{q}} \end{bmatrix} \tag{4.8}$$

Eq. (4.8) shows the *wheel Jacobian* for the n^{th} wheel where

$$\begin{aligned} {}^{v}\mathbf{J}_{\mathrm{n}} &= \mathbf{R}^{\mathrm{d_n}}_{\mathrm{g}}(\mathbf{q}) \\ {}^{\omega}\mathbf{J}_{\mathrm{n}} &= \mathbf{R}^{\mathrm{d_n}}_{\mathrm{g}}(\mathbf{q})[-\mathbf{r}^{\mathrm{g}}_{\mathrm{g,d_n}}\times] \\ {}^{q}\mathbf{J}_{\mathrm{n}} &= \mathbf{R}^{\mathrm{d_n}}_{\mathrm{g}}(\mathbf{q})\ \mathbf{J}_{\mathrm{n}} \end{aligned}$$

It shall be further seen how the longitudinal slip of the wheel is related to its velocity. The **longitudinal** component of wheel velocity can be written as a function of slip and wheel rotation speed from Eq. (4.1).

$$\mathbf{v}^{\mathrm{d_n}}_{\mathrm{i,d_n}} \cdot \hat{\mathbf{x}}_{\mathrm{d_n}} = (1 - s_{\mathrm{n}})\omega_{\mathrm{w_n}} r_{\mathrm{w_n}}$$

The $(\cdot)$ operator refers to the dot product performed on two vectors. $\hat{\mathbf{x}}_{\mathrm{d_n}}$ is the unit vector pointing along the x axis of the n^{th} drive frame. Rearranging Eq. (4.8) for the wheel rate, it can now be written as

$$\begin{bmatrix} \omega_{\mathrm{w_n}} \\ \mathbf{v}^{\mathrm{d_n}}_{\mathrm{i,d_n}} \cdot \hat{\mathbf{y}}_{\mathrm{d_n}} \\ \mathbf{v}^{\mathrm{d_n}}_{\mathrm{i,d_n}} \cdot \hat{\mathbf{z}}_{\mathrm{d_n}} \end{bmatrix} = \begin{bmatrix} \omega_{\mathrm{w_n}} \\ 0 \\ 0 \end{bmatrix} = \begin{bmatrix} \frac{1}{(1-s_{\mathrm{n}})r_{\mathrm{w_n}}} & 0 & 0 \\ 0 & 1 & 0 \\ 0 & 0 & 1 \end{bmatrix} \mathbf{v}^{\mathrm{d_n}}_{\mathrm{i,d_n}} \tag{4.9}$$

Eq. (4.9) gives the wheel rate and y, z components of wheel velocity (assumed to be zero) in the drive frame for the n^{th} wheel. The combined equations for all wheels can be written by clubbing all the wheel rates and, y, z components of the wheel velocities one below the other as

$$\begin{bmatrix} \omega_{\mathrm{w_{FL}}} \\ \omega_{\mathrm{w_{ML}}} \\ \vdots \\ \omega_{\mathrm{w_{FR}}} \\ \mathbf{0}_{6\times1} \\ \mathbf{0}_{6\times1} \end{bmatrix} = \begin{bmatrix} \frac{1}{(1-s_{\mathrm{FL}})r_{\mathrm{w}}} & & & & \\ & \frac{1}{(1-s_{\mathrm{ML}})r_{\mathrm{w}}} & & & \\ & & \ddots & & \mathbf{0}_{6\times12} \\ & & & \frac{1}{(1-s_{\mathrm{FR}})r_{\mathrm{w}}} & \\ & & \mathbf{0}_{12\times6} & & \mathbf{I}_{12\times12} \end{bmatrix} {}^{R}\mathbf{J}(\mathbf{q}) \begin{bmatrix} \mathbf{v}^{\mathrm{g}}_{\mathrm{i,g}} \\ \boldsymbol{\omega}^{\mathrm{g}}_{\mathrm{i,g}} \\ \dot{\mathbf{q}} \end{bmatrix} \tag{4.10}$$

${}^{R}\mathbf{J}$ is the combined wheel Jacobian for all wheels of the rover. Note that in the case of the ExoMars rover all the wheel radii are the same.

4.3 Kinematic equations of motion

The kinematic equations of motion describe the temporal behaviour of the system. The evolution of rover velocity and wheel slip with time is what is of interest here. Therefore these are the states taken into consideration. Additionally the orientation of the rover given by the Euler angles is also taken as a state, the reason for this is explained in Section 4.3.2. The differential kinematic equations of motions describing the rover velocity and orientation for the implementation in the nonlinear Kalman filter are taken from a standard strapdown algorithm (Wendel, 2007). Note that the term *homing* used in the following sections, refers to an initialization of the system done before starting to drive the rover – this includes initializing the gravity vector and calculating the covariances of the sensor measurements.

4.3.1 Rover velocity

The rate of change of rover velocity is the acceleration of the rover which can be measured from the IMU accelerometer. In continuous time, the rate of change of rover velocity can be derived as

$$\begin{aligned}
\dot{\mathbf{r}}^{\mathrm{i}}_{\mathrm{i,g}} &= \mathbf{v}^{\mathrm{i}}_{\mathrm{i,g}} = \mathbf{R}^{\mathrm{i}}_{\mathrm{g}}\mathbf{v}^{\mathrm{g}}_{\mathrm{i,g}} \\
\dot{\mathbf{v}}^{\mathrm{i}}_{\mathrm{i,g}} &= \mathbf{a}^{\mathrm{i}}_{\mathrm{i,g}} = \mathbf{R}^{\mathrm{i}}_{\mathrm{g}}[\boldsymbol{\omega}^{\mathrm{g}}_{\mathrm{i,g}}\times]\mathbf{v}^{\mathrm{g}}_{\mathrm{i,g}} + \mathbf{R}^{\mathrm{i}}_{\mathrm{g}}\dot{\mathbf{v}}^{\mathrm{g}}_{\mathrm{i,g}} \\
\dot{\mathbf{v}}^{\mathrm{g}}_{\mathrm{i,g}} &= -\boldsymbol{\omega}^{\mathrm{g}}_{\mathrm{i,g}} \times \mathbf{v}^{\mathrm{g}}_{\mathrm{i,g}} + \mathbf{a}^{\mathrm{g}}_{\mathrm{i,g}}
\end{aligned} \tag{4.11}$$

$\boldsymbol{\omega}^{\mathrm{g}}_{\mathrm{i,g}}$ is the rotation rate of the rover taken from the IMU gyroscope and $\mathbf{a}^{\mathrm{g}}_{\mathrm{i,g}}$ is the acceleration of the rover which can be taken from the IMU accelerometer. The IMU accelerometer however measures the specific force $\mathbf{f}^{\mathrm{g}}_{\mathrm{i,g}}$ acting on the rover which includes the acceleration due to gravity which needs to be subtracted to get the rover's acceleration as

$$\mathbf{f}^{\mathrm{g}}_{\mathrm{i,g}} = \mathbf{a}^{\mathrm{g}}_{\mathrm{i,g}} + \mathbf{g}^{\mathrm{g}} \tag{4.12}$$

$\mathbf{g}^{\mathrm{g}}$ is calculated by rotating the initialized gravity vector measured during *homing*, $\mathbf{g}^{\mathrm{i}}$ with the Euler angles that determine the roll (ϕ), pitch (θ) and yaw (ψ) of the rover. Substituting Eq. (4.12) into Eq. (4.11)

$$\dot{\mathbf{v}}^{\mathrm{g}}_{\mathrm{i,g}} = -\boldsymbol{\omega}^{\mathrm{g}}_{\mathrm{i,g}} \times \mathbf{v}^{\mathrm{g}}_{\mathrm{i,g}} + \mathbf{f}^{\mathrm{g}}_{\mathrm{i,g}} - \mathbf{R}^{\mathrm{g}}_{\mathrm{i}}\mathbf{g}^{\mathrm{i}} \tag{4.13}$$

The rotation matrix $\mathbf{R}^{\mathrm{g}}_{\mathrm{i}}$ in Eq. (4.13) is a function of (ϕ, θ, ψ) and is derived from Eq. (2.2).

4.3.2 Orientation

In order to compute the rotation matrix in Eq. (4.13) it is required to know how the roll, pitch and yaw evolve with time. Since the attitude of the rover is not available as a direct measurement, it is taken as a state and estimated from the gyroscope measurement. Let the orientation vector be $\boldsymbol{\Theta} = \begin{bmatrix}\psi & \theta & \phi\end{bmatrix}^{\mathrm{T}}$ then the rate of change of Euler angles (refer Section 2.4) is given by Eq. (4.14)

$$\dot{\boldsymbol{\Theta}} = \begin{bmatrix}\dot{\psi}\\ \dot{\theta}\\ \dot{\phi}\end{bmatrix} = \frac{1}{\cos\theta}\begin{bmatrix}0 & \sin\phi & \cos\phi\\ 0 & \cos\theta\cos\phi & -\cos\theta\sin\phi\\ \cos\theta & \sin\theta\sin\phi & \sin\theta\cos\phi\end{bmatrix}\boldsymbol{\omega}^{\mathrm{g}}_{\mathrm{i,g}} \tag{4.14}$$

4.3.3 Wheel slip

The slip is modelled as a damped model as

$$\dot{s}_{\mathrm{n}} = -As_{\mathrm{n}} \tag{4.15}$$

s_{n} is the longitudinal slip of the n^{th} wheel. In the damped model the rate of change of slip is approximated with a factor, $-A$ of the slip value. For smooth terrain driving this is a reasonable assumption since the terrain is assumed to be smooth and therefore would not induce sharp changes in the slippage of the vehicle. The minus sign indicates that the slip stabilizes itself to its nominal value of zero.

The differential kinematics of the rover (Section 4.2) combined with the equations of motion given by the rover velocity, orientation and wheel slip (Section 4.3), cover the entire system model for the rover driving on smooth terrain. Note that the *entire* system model here only refers to the differential kinematics and not ground contact forces and so on. In the following section implementation of the system model within the framework of a nonlinear Kalman filter to estimate the rover velocity and wheel slip is described.

4.4 Filter framework

To implement the Kalman filter the continuous time state equations are discretized with a time step t_s. The discretization is done with a first order solution of the ODEs using Euler method. The uncertainties in the system model and sensor noises are added as Gaussian noise. Fig. 4.3 shows a quick overview of the inputs going into the filter and the state estimates output by the filter.

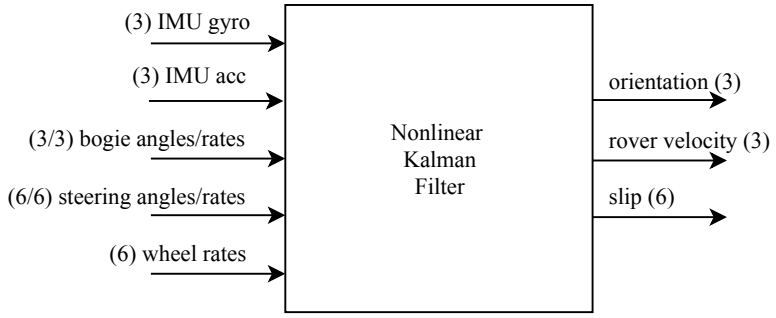

Figure 4.3: Inputs to and outputs from the nonlinear Kalman filter. Numbers in parenthesis show the number of components in each measurement/state.

4.4.1 Sensor noise

Before developing the process and measurement model for the Kalman filter, the sensor models used for the additional inputs in the filter are described. The sensors are modelled with the addition of Gaussian noise with their covariances calculated during the *homing* of the rover. Sensor bias is assumed zero. The sensors used as additional inputs to the filter are the IMU accelerometer and gyroscope, and the potentiometers for joint angles and derived joint rate measurements. The sensor models used are

$$\begin{aligned}
\boldsymbol{\omega}^{\mathrm{g}}_{\mathrm{i,g}}[k] &= \tilde{\boldsymbol{\omega}}^{\mathrm{g}}_{\mathrm{i,g}}[k] - \mathbf{n}_{\omega}[k] \\
\mathbf{f}^{\mathrm{g}}_{\mathrm{i,g}}[k] &= \tilde{\mathbf{f}}^{\mathrm{g}}_{\mathrm{i,g}}[k] - \mathbf{n}_{f}[k] \\
\mathbf{q}[k] &= \tilde{\mathbf{q}}[k] - \mathbf{n}_{q}[k] \\
\dot{\mathbf{q}}[k] &= \tilde{\dot{\mathbf{q}}}[k] - \mathbf{n}_{\dot{q}}[k]
\end{aligned} \tag{4.16}$$

$\tilde{(\bullet)}$ is the measured value from the sensor, from which the noise is subtracted to get the true value and $[k]$ refers to the k^{th} time step. $\mathbf{n}_{\bullet}[k]$ is the noise at the k^{th} time step with a normal distrubition having zero mean and covariance calculated during *homing* of the rover.

4.4.2 Process model

Eqs. (4.11), (4.14) and (4.15) in the discretized form represent the process model of the Kalman filter given below.

$$\begin{aligned}\boldsymbol{\Theta}[k+1] &= \boldsymbol{\Theta}[k] + \dot{\boldsymbol{\Theta}}[k]t_s + \mathbf{n}_\Theta[k] \\ \mathbf{v}^{\mathrm{g}}_{\mathrm{i,g}}[k+1] &= \mathbf{v}^{\mathrm{g}}_{\mathrm{i,g}}[k] + \dot{\mathbf{v}}^{\mathrm{g}}_{\mathrm{i,g}}[k]t_s + \mathbf{n}_v[k] \\ \mathbf{s}[k+1] &= \mathbf{s}[k] + \dot{\mathbf{s}}[k]t_s + \mathbf{n}_s[k] \end{aligned} \tag{4.17}$$

s is the longitudinal slip vector for all wheels combined, $\mathbf{n}_\bullet$ here is the uncertainty associated with ($\bullet$) state and t_s is the time step between two consecutive iterations of the filter. Substituting the sensor noise models in Eq. (4.16) into Eqs. (4.11), (4.14) and (4.15), their discretized form is given below.

$$\begin{aligned}&\dot{\boldsymbol{\Theta}}[k] = \\ &\frac{1}{\cos\theta[k]}\begin{bmatrix} 0 & \sin\phi[k] & \cos\phi[k] \\ 0 & \cos\theta[k]\cos\phi[k] & -\cos\theta[k]\sin\phi[k] \\ \cos\theta[k] & \sin\theta[k]\sin\phi[k] & \sin\theta[k]\cos\phi[k] \end{bmatrix}(\tilde{\boldsymbol{\omega}}^{\mathrm{g}}_{\mathrm{i,g}}[k] - \mathbf{n}_\omega[k]) \\ &\dot{\mathbf{v}}^{\mathrm{g}}_{\mathrm{i,g}}[k] = -(\tilde{\boldsymbol{\omega}}^{\mathrm{g}}_{\mathrm{i,g}}[k] - \mathbf{n}_\omega[k]) \times \mathbf{v}^{\mathrm{g}}_{\mathrm{i,g}}[k] + \tilde{\mathbf{f}}^{\mathrm{g}}_{\mathrm{i,g}}[k] - \mathbf{n}_f[k] - \mathbf{R}^{\mathrm{g}}_{\mathrm{i}}[k]\mathbf{g}^{\mathrm{i}} \\ &\dot{\mathbf{s}}[k] = -\mathbf{A}\mathbf{s}[k] \end{aligned} \tag{4.18}$$

Therefore the process model is of the form

$$\mathbf{x}[k+1] = \mathbf{f}(\mathbf{x}[k], \mathbf{n}_p[k], \mathbf{u}_p[k]) \tag{4.19}$$

where **f** is the state transition function and

$$\mathbf{x} = \begin{bmatrix} \boldsymbol{\Theta} \\ \mathbf{v}^{\mathrm{g}}_{\mathrm{i,g}} \\ \mathbf{s} \end{bmatrix}, \mathbf{u}_p = \begin{bmatrix} \tilde{\boldsymbol{\omega}}^{\mathrm{g}}_{\mathrm{i,g}} \\ \tilde{\mathbf{f}}^{\mathrm{g}}_{\mathrm{i,g}} \\ \mathbf{g}^{\mathrm{i}} \end{bmatrix}, \mathbf{n}_p = \begin{bmatrix} \mathbf{n}_\Theta \\ \mathbf{n}_v \\ \mathbf{n}_s \\ \mathbf{n}_f \\ \mathbf{n}_\omega \end{bmatrix}$$

4.4.3 Measurement model

Eq. (4.10) is taken as the measurement model for the Kalman filter where the wheel rates measured from the encoders are one set of measurements, and the y and z components of the wheel velocity in the drive frame assumed to be zero for smooth driving terrain, are taken as the second set of measurements. Substituting the sensor noise models in Eq. (4.16) into Eq. (4.10), the discretized form is given below.

$$\begin{bmatrix} \omega_{\mathrm{w_{FL}}} \\ \omega_{\mathrm{w_{ML}}} \\ \vdots \\ \omega_{\mathrm{w_{FR}}} \\ \mathbf{0}_{6\times1} \\ \mathbf{0}_{6\times1} \end{bmatrix}_{[k]} = \begin{bmatrix} \frac{1}{(1-s_{\mathrm{FL}})r_{\mathrm{w}}} & & & & \\ & \frac{1}{(1-s_{\mathrm{ML}})r_{\mathrm{w}}} & & & \mathbf{0}_{6\times12} \\ & & \ddots & & \\ & & & \frac{1}{(1-s_{\mathrm{FR}})r_{\mathrm{w}}} & \\ & \mathbf{0}_{12\times6} & & & \mathbf{I}_{12\times12} \end{bmatrix}_{[k]} \tag{4.20}$$
$$ {}^{R}\mathbf{J}(\tilde{\mathbf{q}}[k] - \mathbf{n}_q[k]) \begin{bmatrix} \mathbf{v}^{\mathrm{g}}_{\mathrm{i,g}} \\ \tilde{\boldsymbol{\omega}}^{\mathrm{g}}_{\mathrm{i,g}} - \mathbf{n}_\omega \\ \dot{\tilde{\mathbf{q}}} - \mathbf{n}_{\dot{q}} \end{bmatrix}_{[k]} + \begin{bmatrix} \mathbf{n}_{\mathrm{w}} \\ \mathbf{n}_{v_y} \\ \mathbf{n}_{v_z} \end{bmatrix}_{[k]} $$

$\mathbf{n}_{\mathrm{w}}$ is the noise associated with wheel encoder measurements with a normal distribution whose covariance is calculated during *homing*. $\mathbf{n}_{v_y}, \mathbf{n}_{v_z}$ are the uncertainties associated with the modelling of the kinematics. Therefore the measurement model is of the form,

$$\mathbf{y}[k] = \mathbf{h}(\mathbf{x}[k], \mathbf{n}_m[k], \mathbf{u}_m[k]) \tag{4.21}$$

where **h** is the measurement function and

$$\mathbf{y} = \begin{bmatrix} \boldsymbol{\omega}_{\mathrm{w}} \\ \mathbf{0} \\ \mathbf{0} \end{bmatrix}, \mathbf{u}_m = \begin{bmatrix} \tilde{\boldsymbol{\omega}}^{\mathrm{g}}_{\mathrm{i,g}} \\ \tilde{\mathbf{q}} \\ \dot{\tilde{\mathbf{q}}} \end{bmatrix}, \mathbf{n}_m = \begin{bmatrix} \mathbf{n}_\omega \\ \mathbf{n}_{\mathrm{w}} \\ \mathbf{n}_q \\ \mathbf{n}_{\dot{q}} \\ \mathbf{n}_{v_y} \\ \mathbf{n}_{v_z} \end{bmatrix}$$

Now that the sensor models, process model and measurement model have been set up in the standard filter framework, the implementation settings are presented in the following section.

4.5 Filter implementation

From the process and measurement model it can be seen that the system has nonlinearities (discussed in more detail in Section 5.7) and therefore a nonlinear Kalman filter like the extended (EKF) or unscented Kalman filter (UKF) needs to be implemented to estimate the states of the system. MATLAB has predefined classes that implement the two filters and the functions `extendedKalmanFilter()` and `unscentedKalmanFilter()` allow objects of these classes to be created.

By creating an object of the class, certain properties of the filter can be set and the `predict()` and `correct()` functions, which perform the predict and update step (refer Sections 2.5.1 and 2.5.2) of the Kalman filter respectively, can be called with the object.

Filter properties:

1. **State transition function** - is the function **f** taken from Eq. (4.19)
2. **Measurement function** - is the function **h** taken from Eq. (4.21)
3. **Initial state** - is set to the best guess of the state at time $t = 0$ i.e. $\mathbf{x}(0)$
4. **Initial state error covariance** - is a diagonal matrix with covariances representing the confidence in the initial state guess
5. **Process noise covariance** - is the covariance associated with the vector $\mathbf{n}_p$ taken from Eq. (4.19), calculated during *homing*.
6. **Measurement noise covariance** - is the covariance associated with the vector $\mathbf{n}_m$ taken from Eq. (4.21), calculated during *homing*.
7. **Process noise characteristics** - is taken as *non-additive* since the augmented process noise covariance matrix includes noises associated with the $\mathbf{u}_p$ terms which are handled in a non-additve manner within the state transition function
8. **Measurement noise characteristics** - is taken as *non-additive* since the augmented measurement noise covariance matrix includes noises associated with the $\mathbf{u}_m$ terms which are handled in a non-additve manner within the measurement function

Once the filter properties are set the `predict()` and `correct()` functions are called with the concerned filter object and the additional inputs $\mathbf{u}_p$ and $\mathbf{u}_m$ are passed as arguments.

4.6 Filter drift & limitation of measurement equation

It is a common problem with the Kalman filter estimates that the velocity estimates accumulate errors as the state equation for it is nothing but an integration of the IMU accelerometer readings which are noisy. The drawback of the measurement model is that it is unable to constrain the velocity and slip. The rover Jacobian has a rank deficiency when all wheels are parallel. Therefore the correct step, which

uses the measurement equation, is not able to determine how much of the error is to be weighted to the velocity and how much to the slip, in a unique way. Therefore depending on the scenario and the noise in the measurements the performance of the filter can vary. It is left to the predict step to make a reliable prediction which depends on how accurately the process states are modelled. There can be several inaccuracies in the state equation related to the rover velocity, for example, the gyroscope bias is assumed zero or the initialization of the gravity vector may be inaccurate. Also, the wheel slip is modelled as a damped model which is a stochastic guess. The choice of covariance for the various states effects the Kalman gain computation which determines how much of the predicted states to trust in comparison with those from the update step. Defining the right covariances for the model uncertainties is a common challenge in Kalman filtering.

This chapter completes the description of the existing framework of estimation of rover velocity and wheel slip for smooth terrain. The following chapter introduces the contact angle and additionally a side slip angle, which are then integrated into the existing framework to estimate them together with the rover velocity and wheel slips for rough terrain.

Chapter 5

Extension of estimator to uneven terrain

The rover kinematics and equations of motion developed so far were for vehicle travel over a smooth terrain where the assumption that the lateral and vertical components of the wheel velocity are zero, was reasonable. However for travel over uneven terrain, this assumption does not hold true and therefore additional variables are needed to account for the lateral and vertical components of velocity imposed on the wheel by the unevenness of the terrain. In this chapter these additional variables needed to fully capture the wheel velocity in three dimensions shall be defined.

Section 5.1 defines the contact angle, which is used to account for the vertical component of the wheel velocity and Section 5.2 defines the side slip angle which accounts for the lateral component. Following the definition of the two additional variables, the longitudinal wheel slip is redefined in Section 5.3 and the kinematics to arrive at the wheel Jacobian are developed in Section 5.4. Section 5.5 presents the extended equations of motion and Section 5.6 summarizes the changes made to the extended filter framework and implementation. Finally a review of the non-linearity of the system equations is presented in Section 5.7.

5.1 Contact angle

The angle in the wheel plane between the normal to the steering axis and the direction of wheel velocity is defined as the contact angle (refer Fig. 5.1). $\mathbf{v}$ is the total wheel velocity.

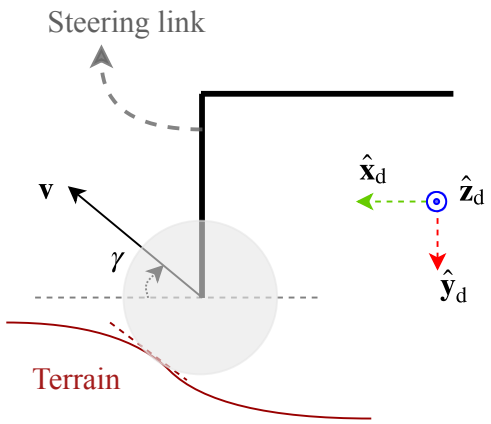

Figure 5.1: Definition of contact angle

With respect to the drive frame, the contact angle can be written as

$$\gamma = \tan^{-1} \frac{-\mathbf{v} \cdot \hat{\mathbf{y}}_d}{\mathbf{v} \cdot \hat{\mathbf{x}}_d}$$

A new frame called the *contact frame* denoted by 'c' is defined. This is obtained by rotating the drive frame about its z axis by the contact angle γ to align the x axis of the new contact frame with the direction of wheel velocity in the wheel rolling plane. Note that a positive contact angle is defined for a negative rotation about $\hat{\mathbf{z}}_c$ axis such that an *'upward'* wheel velocity leads to a positive contact angle and a *'downward'* wheel velocity to a negative contact angle. Additionally a rotation of 90° about the transformed x axis is done to keep the z axis of the contact frame aligned with the axis of side slip rotation in keeping with the DH convention (refer Section 5.4). For the assumption that the lateral component of wheel velocity is zero, velocities in the contact frame can be summarized as,

$$\begin{aligned} \mathbf{v}^c_{i,c} \cdot \hat{\mathbf{x}}_c \cos\gamma &= \mathbf{v} \cdot \hat{\mathbf{x}}_d \\ \mathbf{v}^c_{i,c} \cdot \hat{\mathbf{y}}_c &= 0 \\ \mathbf{v}^c_{i,c} \cdot \hat{\mathbf{z}}_c &= 0 \end{aligned} \tag{5.1}$$

If a lateral component of wheel velocity is considered then $\mathbf{v}^c_{i,c} \cdot \hat{\mathbf{y}}_c \neq 0$. The definition of contact angle has a **singularity** at $\gamma = \pm 90^\circ$ i.e. when the x component of the wheel velocity in drive frame is zero. This corresponds to wheels moving

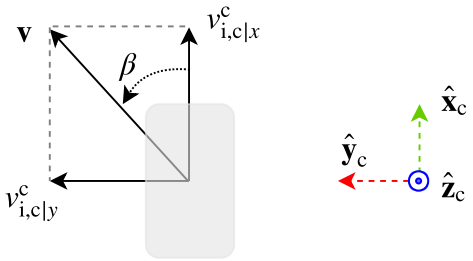

Figure 5.2: Definition of side slip angle

purely in the direction of steering axis. This occurs when the entire bogie is moving upward or downward in the bogie frame or, when the front bogies are in pure rotation about the center of line joining wheel centers with no translational motion.

5.2 Side slip angle

The angle between the wheel velocity and the wheel plane as seen from the top view of the *contact frame* of the wheel is defined as the side slip angle (refer Fig. 5.2). Note that the notation $v^{c}_{i,c|x}$ is equivalent to $\mathbf{v}^{c}_{i,c} \cdot \hat{\mathbf{x}}_c$. These two notations shall be used interchangeable henceforth. The side slip angle with respect to the contact frame is

$$\beta = \tan^{-1} \frac{\mathbf{v} \cdot \hat{\mathbf{y}}_c}{\mathbf{v} \cdot \hat{\mathbf{x}}_c}$$

A new frame called the *side slip frame* denoted by 'ss', is introduced by rotating the contact frame about its z axis by the side slip angle β. A positive side slip angle is defined for a positive rotation about the $\hat{\mathbf{z}}_{ss}$ axis corresponding to a *leftward* wheel velocity as seen from the top view and a negative side slip angle corresponds to a *rightward* wheel velocity. The wheel velocity in the side slip frame can be summarized as

$$\begin{aligned} \mathbf{v}^{ss}_{i,ss} \cdot \hat{\mathbf{x}}_{ss} &= |\mathbf{v}| \\ \mathbf{v}^{ss}_{i,ss} \cdot \hat{\mathbf{x}}_{ss} \cos\beta &= \mathbf{v}^{c}_{i,c} \cdot \hat{\mathbf{x}}_c \\ \mathbf{v}^{ss}_{i,ss} \cdot \hat{\mathbf{y}}_c &= 0 \\ \mathbf{v}^{ss}_{i,ss} \cdot \hat{\mathbf{z}}_c &= 0 \end{aligned} \tag{5.2}$$

The definition of side slip angle has a **singularity** similar to the contact angles when the x component of the wheel velocity in the drive frame is zero. The singu-

larity in this case is cascaded. If there exists only a z component of wheel velocity in the drive frame, this corresponds to a motion of the wheel purely perpendicular to the wheel plane. Here the side slip angle should be 90° but since the side slip angle is defined in the contact frame and the singularity is cascaded, the side slip angle becomes undefined.

5.3 Longitudinal wheel slip

In the previous chapter the longitudinal wheel slip was defined with respect to the x component of wheel velocity in the drive frame. This definition holds for the assumption that the lateral and vertical wheel velocities are zero. As this chapter deals with motion on uneven terrain, the rover has non-zero lateral and vertical wheel velocities. The longitudinal wheel slip in this case is redefined as the ratio of slip speed to pure rolling speed in the *effective* direction of wheel velocity in the wheel plane. Therefore the longitudinal slip is now defined with respect to the x component of wheel velocity in the contact frame regardless of whether the lateral component is non-zero or not.

$$\mathbf{v}_{\mathrm{i,c}}^{\mathrm{c}} \cdot \hat{\mathbf{x}}_{\mathrm{c}} = (1 - s)\omega_{\mathrm{w}} r_{\mathrm{w}}$$

From Eq. (5.2) the longitudinal slip can be related to the wheel velocity in the side slip frame via the side slip angle as

$$\mathbf{v}_{\mathrm{i,ss}}^{\mathrm{ss}} \cdot \hat{\mathbf{x}}_{\mathrm{ss}} = \frac{(1 - s)\omega_{\mathrm{w}} r_{\mathrm{w}}}{\cos \beta} = |\mathbf{v}|$$

The singularities associated with the longitudinal slip definition have already been discussed in the previous chapter.

5.4 Extended wheel Jacobian

The equations developed previously in Section 4.2 are modified to incorporate the contact angle and side slip angle to arrive at the kinematic Jacobian for a single wheel. Two separate models are developed - one considering only contact angle where it is assumed that lateral wheel velocity is zero, and the second considering both the contact and side slip angle where the lateral wheel velocity is also taken into account. A summary of the equations leading up to the wheel Jacobian for the two models is presented in Table 5.1

The wheel Jacobian can be extended to include all six wheels using the extended DH table shown in Table 5.2 as done in Chapter 4. The rover Jacobian in this case

Table 5.1: Kinematics leading to the wheel Jacobian for *contact angle model* and *contact & side slip angle model* for a single wheel

Contact angle model	**Contact & Side slip angle model**
$\mathbf{v}^{\mathrm{c}}_{\mathrm{i,c}} = \mathbf{R}^{\mathrm{c}}_{\mathrm{g}}\mathbf{v}^{\mathrm{g}}_{\mathrm{i,g}} + \mathbf{R}^{\mathrm{c}}_{\mathrm{g}}[\boldsymbol{\omega}^{\mathrm{g}}_{\mathrm{i,g}}\times]\mathbf{r}^{\mathrm{g}}_{\mathrm{g,c}} + \mathbf{R}^{\mathrm{c}}_{\mathrm{g}}\mathbf{v}^{\mathrm{g}}_{\mathrm{g,c}}$	$\mathbf{v}^{\mathrm{ss}}_{\mathrm{i,ss}} = \mathbf{R}^{\mathrm{ss}}_{\mathrm{g}}\mathbf{v}^{\mathrm{g}}_{\mathrm{i,g}} + \mathbf{R}^{\mathrm{ss}}_{\mathrm{g}}[\boldsymbol{\omega}^{\mathrm{g}}_{\mathrm{i,g}}\times]\mathbf{r}^{\mathrm{g}}_{\mathrm{g,ss}} + \mathbf{R}^{\mathrm{ss}}_{\mathrm{g}}\mathbf{v}^{\mathrm{g}}_{\mathrm{g,ss}}$
$\mathbf{R}^{\mathrm{c}}_{\mathrm{g}} = \mathbf{R}^{\mathrm{c}}_{\mathrm{d}}(\gamma)\mathbf{R}^{\mathrm{d}}_{\mathrm{s}}(q_{\mathrm{s}})\mathbf{R}^{\mathrm{s}}_{\mathrm{b}}(q_{\mathrm{b}})\mathbf{R}^{\mathrm{b}}_{\mathrm{g}}$	$\mathbf{R}^{\mathrm{ss}}_{\mathrm{g}} = \mathbf{R}^{\mathrm{ss}}_{\mathrm{c}}(\beta)\mathbf{R}^{\mathrm{c}}_{\mathrm{d}}(\gamma)\mathbf{R}^{\mathrm{d}}_{\mathrm{s}}(q_{\mathrm{s}})\mathbf{R}^{\mathrm{s}}_{\mathrm{b}}(q_{\mathrm{b}})\mathbf{R}^{\mathrm{b}}_{\mathrm{g}}$
$\mathbf{T}^{\mathrm{g}}_{\mathrm{g,c}} = \begin{bmatrix}\mathbf{R}^{\mathrm{g}}_{\mathrm{c}} & \mathbf{r}^{\mathrm{g}}_{\mathrm{g,c}}\\ \mathbf{0} & 1\end{bmatrix}$	$\mathbf{T}^{\mathrm{g}}_{\mathrm{g,ss}} = \begin{bmatrix}\mathbf{R}^{\mathrm{g}}_{\mathrm{ss}} & \mathbf{r}^{\mathrm{g}}_{\mathrm{g,ss}}\\ \mathbf{0} & 1\end{bmatrix}$
$\mathbf{v}^{\mathrm{g}}_{\mathrm{g,c}} = \dfrac{\partial \mathbf{r}^{\mathrm{g}}_{\mathrm{g,c}}}{\partial \mathbf{q}}\,\dot{\mathbf{q}} = \mathbf{J}\,\dot{\mathbf{q}}$	$\mathbf{v}^{\mathrm{g}}_{\mathrm{g,ss}} = \dfrac{\partial \mathbf{r}^{\mathrm{g}}_{\mathrm{g,ss}}}{\partial \mathbf{q}}\,\dot{\mathbf{q}} = \mathbf{J}\,\dot{\mathbf{q}}$
$\mathbf{q} = \begin{bmatrix} q_{\mathrm{b}} & q_{\mathrm{s}} & \gamma\end{bmatrix}^{\mathrm{T}}$	$\mathbf{q} = \begin{bmatrix} q_{\mathrm{b}} & q_{\mathrm{s}} & \gamma & \beta\end{bmatrix}^{\mathrm{T}}$
$\mathbf{v}^{\mathrm{c}}_{\mathrm{i,c}} = \begin{bmatrix}{}^{v}\mathbf{J} & {}^{\omega}\mathbf{J} & {}^{q}\mathbf{J}\end{bmatrix}\begin{bmatrix}\mathbf{v}^{\mathrm{g}}_{\mathrm{i,g}}\\ \boldsymbol{\omega}^{\mathrm{g}}_{\mathrm{i,g}}\\ \dot{\mathbf{q}}\end{bmatrix}$	$\mathbf{v}^{\mathrm{ss}}_{\mathrm{i,ss}} = \begin{bmatrix}{}^{v}\mathbf{J} & {}^{\omega}\mathbf{J} & {}^{q}\mathbf{J}\end{bmatrix}\begin{bmatrix}\mathbf{v}^{\mathrm{g}}_{\mathrm{i,g}}\\ \boldsymbol{\omega}^{\mathrm{g}}_{\mathrm{i,g}}\\ \dot{\mathbf{q}}\end{bmatrix}$
${}^{v}\mathbf{J} = \mathbf{R}^{\mathrm{c}}_{\mathrm{g}}(\mathbf{q})$	${}^{v}\mathbf{J} = \mathbf{R}^{\mathrm{ss}}_{\mathrm{g}}(\mathbf{q})$
${}^{\omega}\mathbf{J} = \mathbf{R}^{\mathrm{c}}_{\mathrm{g}}(\mathbf{q})[-\mathbf{r}^{\mathrm{g}}_{\mathrm{g,d}}\times]$	${}^{\omega}\mathbf{J} = \mathbf{R}^{\mathrm{ss}}_{\mathrm{g}}(\mathbf{q})[-\mathbf{r}^{\mathrm{g}}_{\mathrm{g,d}}\times]$
${}^{q}\mathbf{J} = \mathbf{R}^{\mathrm{c}}_{\mathrm{g}}(\mathbf{q})\,\mathbf{J}$	${}^{q}\mathbf{J} = \mathbf{R}^{\mathrm{ss}}_{\mathrm{g}}(\mathbf{q})\,\mathbf{J}$
$\mathbf{v}^{\mathrm{c}}_{\mathrm{i,c}}\cdot\hat{\mathbf{x}}_{\mathrm{c}} = (1-s)\omega_{\mathrm{w}}r_{\mathrm{w}}$	$\mathbf{v}^{\mathrm{ss}}_{\mathrm{i,ss}}\cdot\hat{\mathbf{x}}_{\mathrm{ss}} = \dfrac{(1-s)\omega_{\mathrm{w}}r_{\mathrm{w}}}{\cos\beta}$
$\begin{bmatrix}\omega_{\mathrm{w}}\\ 0\\ 0\end{bmatrix} = \begin{bmatrix}\frac{1}{(1-s)r_{\mathrm{w}}} & 0 & 0\\ 0 & 1 & 0\\ 0 & 0 & 1\end{bmatrix}\mathbf{v}^{\mathrm{c}}_{\mathrm{i,c}}$	$\begin{bmatrix}\omega_{\mathrm{w}}\\ 0\\ 0\end{bmatrix} = \begin{bmatrix}\frac{\cos\beta}{(1-s)r_{\mathrm{w}}} & 0 & 0\\ 0 & 1 & 0\\ 0 & 0 & 1\end{bmatrix}\mathbf{v}^{\mathrm{ss}}_{\mathrm{i,ss}}$

would include the additional rotation matrices that transform the wheel velocities to the contact frame and the side slip frame respectively in the corresponding models described in Table 5.1.

5.5 Extended equations of motion

The evolution of rover velocity, orientation and wheel slip with time was covered in Section 4.3. In addition to these states of the system, two additional states for the contact and side slip angles need to be developed. In Section 3.2.2 two state models for the contact angle were discussed. A *random walk* was used in (Iagnemma et al., 2004) and a *damped model* in (Balaram, 2000) to model the contact

Table 5.2: DH table continued from table 4.2

Link	θ_i	d_i	a_i	α_i
(contd.)...	...	...	...	...
$\mathrm{d_{FL}} \rightarrow \mathrm{c_{FL}}$	$-\gamma_{\mathrm{FL}}$	0.0000	0.0000	$\pi/2$
$\mathrm{d_{ML}} \rightarrow \mathrm{c_{ML}}$	$-\gamma_{\mathrm{ML}}$	0.0000	0.0000	$\pi/2$
$\mathrm{d_{RL}} \rightarrow \mathrm{c_{RL}}$	$-\gamma_{\mathrm{RL}}$	0.0000	0.0000	$\pi/2$
$\mathrm{d_{RR}} \rightarrow \mathrm{c_{RR}}$	$-\gamma_{\mathrm{RR}}$	0.0000	0.0000	$\pi/2$
$\mathrm{d_{MR}} \rightarrow \mathrm{c_{MR}}$	$-\gamma_{\mathrm{MR}}$	0.0000	0.0000	$\pi/2$
$\mathrm{d_{FR}} \rightarrow \mathrm{c_{FR}}$	$-\gamma_{\mathrm{FR}}$	0.0000	0.0000	$\pi/2$
$\mathrm{c_{FL}} \rightarrow \mathrm{ss_{FL}}$	β_{FL}	0.0000	0.0000	0
$\mathrm{c_{ML}} \rightarrow \mathrm{ss_{ML}}$	β_{ML}	0.0000	0.0000	0
$\mathrm{c_{RL}} \rightarrow \mathrm{ss_{RL}}$	β_{RL}	0.0000	0.0000	0
$\mathrm{c_{RR}} \rightarrow \mathrm{ss_{RR}}$	β_{RR}	0.0000	0.0000	0
$\mathrm{c_{MR}} \rightarrow \mathrm{ss_{MR}}$	β_{MR}	0.0000	0.0000	0
$\mathrm{c_{FR}} \rightarrow \mathrm{ss_{FR}}$	β_{FR}	0.0000	0.0000	0

angle state. The same model used for contact angle state shall be used to model the side slip angle state.

Damped model:

$$\begin{aligned} \dot{\gamma}_{\mathrm{n}} &= -A_{\gamma}\gamma_{\mathrm{n}} + \tilde{n}_{\gamma} \\ \dot{\beta}_{\mathrm{n}} &= -A_{\beta}\beta_{\mathrm{n}} + \tilde{n}_{\beta} \end{aligned} \tag{5.3}$$

Random walk:

$$\begin{aligned} \dot{\gamma}_{\mathrm{n}} &= \tilde{n}_{\gamma} \\ \dot{\beta}_{\mathrm{n}} &= \tilde{n}_{\beta} \end{aligned} \tag{5.4}$$

Eqs. (5.3) and (5.4) are the state equations for a damped model and random walk. γ_{n} and β_{n} are the contact and side slip angles for the n^{th} wheel respectively. $A_{\bullet}$ is a damping parameter and $\tilde{n}_{\bullet}$ is the Gaussian noise associated with ($\bullet$) state.

5.6 Extended filter framework & implementation

The Kalman filter framework is the same as in Section 4.4 but with the addition of the extended states given by Eq. (5.3) or Eq. (5.4) depending on the choice of state model. The sensor noise models, process model and measurement model are

extended to include the contact and side slip angles.

$$\boldsymbol{\gamma}[k+1] = \boldsymbol{\gamma}[k] + \dot{\boldsymbol{\gamma}}[k]t_s + \mathbf{n}_{\gamma}[k] \tag{5.5}$$

$$\boldsymbol{\beta}[k+1] = \boldsymbol{\beta}[k] + \dot{\boldsymbol{\beta}}[k]t_s + \mathbf{n}_{\beta}[k] \tag{5.6}$$

In addition to the process model in Eq. (4.17), for the *contact angle model* Eq. (5.5) is incorporated and for the *contact & side slip angle model* both Eqs. (5.5) and (5.6) are incorporated. Note that the noise terms in Eqs. (5.5) and (5.6) are equivalent to the $\tilde{n}_{\bullet}$ term in Eqs. (5.3) and (5.4) multiplied by a factor equal to the time step t_s. $\boldsymbol{\gamma}$ is the contact angle vector and $\boldsymbol{\beta}$ the side slip angle vector for all wheels combined. Similarly the appropriate measurement equations from Table 5.1 are used for the *contact angle model* and *contact & side slip angle model*.

Fig. 5.3 shows the filter inputs and outputs as in Section 4.4 with the addition of the extended states. As the process and measurement models of the extended filter framework also have nonlinearities, a nonlinear Kalman filter like the EKF or UKF can be used to estimate the states. A short study on the nonlinearity of the system is presented in the following section.

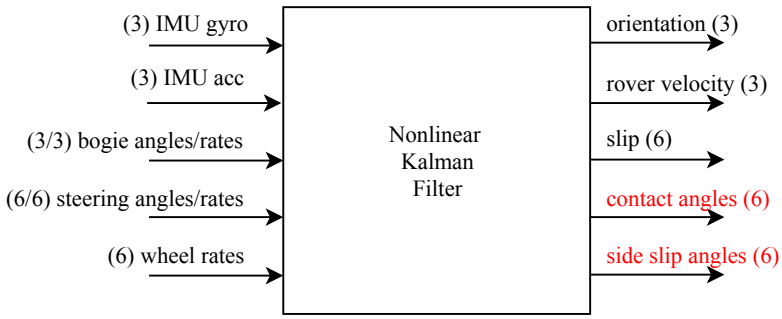

Figure 5.3: Filter framework with extended states

5.7 Study of nonlinearity of the system

The EKF algorithm linearizes the state transition and measurement function about the current state. The linearization of both the state transition and measurement function is done with respect to the state vector and the noise vector (refer Section 2.5.1). Therefore these Jacobians are what are of interest to see if they represent good linearizations of the system or not. The linearization works well for moderately nonlinear systems if the variation in state is small in the time step of

linearization considered. However it may lead to divergence of the filter for highly nonlinear systems since the variation in state may be large over the time step of linearization considered. The system equations considered here are for the *contact & side slip angle model*.

A moderately nonlinear function is one which has no discontinuities or sharp changes in the output for the variation of states within the step size of discretization considered. Fig. 5.4 shows the difference between a moderately nonlinear and highly nonlinear system.

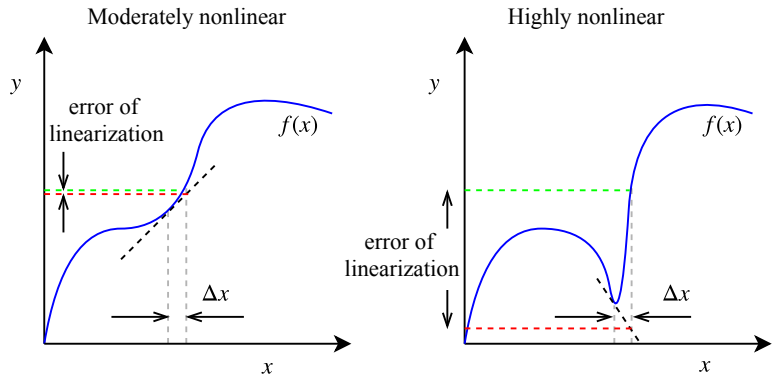

Figure 5.4: Nonlinear systems. Adapted from Mathworks:Understanding Kalman Filters

In the EKF algorithm the four Jacobians used are

$$\mathbf{F} = \left.\frac{\partial \mathbf{f}}{\partial \mathbf{x}}\right|_{\mathbf{x}[k],\bar{\mathbf{n}}_p,\mathbf{u}_p[k]} \text{ and } \mathbf{L} = \left.\frac{\partial \mathbf{f}}{\partial \mathbf{n}_p}\right|_{\mathbf{x}[k],\bar{\mathbf{n}}_p,\mathbf{u}_p[k]}$$

$$\mathbf{H} = \left.\frac{\partial \mathbf{h}}{\partial \mathbf{x}}\right|_{\mathbf{x}[k],\bar{\mathbf{n}}_m,\mathbf{u}_m[k]} \text{ and } \mathbf{M} = \left.\frac{\partial \mathbf{h}}{\partial \mathbf{n}_m}\right|_{\mathbf{x}[k],\bar{\mathbf{n}}_m,\mathbf{u}_m[k]}$$

The idea is to understand the nonlinearities of the system to see if these Jacobians can make good approximations of the state transition and measurement functions. Table 5.3 summarizes the nonlinearities of the functions **f** and **h** with respect to the variables $\mathbf{x}, \mathbf{n}_p$ and $\mathbf{n}_m$. In the process model keeping $\mathbf{u}_p$ and $\mathbf{n}_p$ constant the nonlinearities associated with the state transition function **f** are summarized below.

- Euler angles vary nonlinearly because of the trigonometric functions associated with them
- The rover velocity varies nonlinearly because of the term $\mathbf{R}_i^g$ depends nonlinearly on the Euler angles.

Table 5.3: Overview of system nonlinearities

$\mathbf{x}$	$\mathbf{f}$	$\mathbf{h}$	$\mathbf{n}_p$	$\mathbf{f}$	$\mathbf{n}_m$	$\mathbf{h}$
Θ	✓	-	$\mathbf{n}_\Theta$	×	$\mathbf{n}_\omega$	×
$\mathbf{v}_{\mathrm{i,g}}^{\mathrm{g}}$	✓	×	$\mathbf{n}_v$	×	$\mathbf{n}_{\mathrm{w}}$	×
$\mathbf{s}$	×	✓	$\mathbf{n}_s$	×	$\mathbf{n}_q$	✓
$\boldsymbol{\gamma}$	×	✓	$\mathbf{n}_\gamma$	×	$\mathbf{n}_{\dot{q}}$	×
$\boldsymbol{\beta}$	×	✓	$\mathbf{n}_\beta$	×	$\mathbf{n}_{v_y}$	×
			$\mathbf{n}_f$	×	$\mathbf{n}_{v_z}$	×
			$\mathbf{n}_\omega$	×		

✓ - *function* in column has nonlinearity associated with *variable* in row.
× - *function* in column has no nonlinearity associated with *variable* in row.

- The wheel slip, contact and side slip angles vary linearly.

Similarly, keeping $\mathbf{x}$ and $\mathbf{u}_p$ constant, state transition function $\mathbf{f}$ varies linearly with the noise vector $\mathbf{n}_p$.

In the measurement model keeping $\mathbf{u}_m$ and $\mathbf{n}_m$ constant the nonlinearities associated with the measurement function $\mathbf{h}$ are summarized below.

- The wheel rates vary nonlinearly with the wheel slip as a $1/(1-s)$ function
- The wheel rates, $\mathbf{v}_{\mathrm{i,ss}|x}^{\mathrm{ss}}$ and $\mathbf{v}_{\mathrm{i,ss}|y}^{\mathrm{ss}}$ also vary nonlinearly with the contact and side slip angles due to trigonometric functions associated with them in the rover Jacobian ${}^{R}\mathbf{J}$
- The rover velocity $\mathbf{v}_{\mathrm{i,g}}^{\mathrm{g}}$ varies linearly

Similarly, keeping $\mathbf{x}$ and $\mathbf{u}_m$ constant, measurement function $\mathbf{h}$ varies linearly with all components of the noise vector $\mathbf{n}_m$ except $\mathbf{n}_q$ which varies nonlinearly as trigonometric functions are associated with them in the rover Jacobian ${}^{R}\mathbf{J}$.

The four Jacobians used in the EKF algorithm have several trigonometric functions associated with the rotation matrices involved. The Euler angles have a singularity when the pitch $\theta = \frac{\pi}{2}$. Trigonometric functions are nonlinear functions with the sinus and cosine functions continuous and differentiable in the range $(-\pi, +\pi)$ and tangent in the range $(-\frac{\pi}{2}, +\frac{\pi}{2})$. The period of sinus and cosine is 2π and that of tangent is π. In the trigonometric expressions involved in the state transition function and the measurement function, the period of the arithmetically combined sinus and cosine functions is still 2π. This is a very low frequency associated with

the nonlinearity since for the time step considered in the filter (1 millisecond), the change in state $\mathbf{x}$ would be very small such that the nonlinearity could be easily approximated with a linearization.

In the discussion above, $\mathbf{u}_p$ and $\mathbf{u}_m$ were considered constant. However this is actually not the case as these inputs are time-varying parameters and some of them even vary nonlinearly. This makes the analysis of nonlinearity more complex. However as mentioned earlier, the time step of the filter is small enough that large changes in $\mathbf{u}_p$ and $\mathbf{u}_m$ are not expected in that time step. The true feasibility of the EKF filter in handling the nonlinear system dynamics can be seen when a test scenario is taken and the results compared from those obtained from a UKF (discussed in the following chapter).

Now that the extended estimator for rough terrain has been set up in this chapter, the results and analysis of estimation for a few test scenarios is presented in the following chapter.

Chapter 6

Results and verification

In this chapter two steps are followed for the verification of the contact and side slip angle estimation using the extended framework developed in Chapter 5. The first step is a verification of the estimator against hypothetical scenarios with artificial measurements and the second step is a verification of the estimator against tests conducted in the lab with real measurements. Note that all estimation results presented here are performed **offline**.

A brief discussion on the reference signals generated to compare the estimates against, is discussed in Section 6.1. Remarks on the choice of results presented in the subsequent sections and some filter settings are listed in Section 6.2. Section 6.3 and Section 6.4 present the hypothetical scenarios to verify contact angle estimation and the side slip angle estimation respectively. Section 6.5 further presents the results of the estimator when applied to a lab test conducted specially to study the development of contact angles and Section 6.6 for a lab test that focuses on the side slip angles. A thorough understanding of the test scenarios is presented to be able to anticipate intuitively what the estimates must look like before discussing the estimation results.

6.1 Generating reference

In order to be able to verify the results of the estimation a reliable reference signal is needed. To generate the reference for rover velocity, wheel slip, contact and side slip angles in case of hypothetical scenarios is straightforward since in the ideal scenarios the ideal rover velocity and wheel rates are taken, from which the contact angles, side slip angles and wheel slip are computed using the kinematic relations.

For the tests conducted in the lab, the reference velocity of the rover is determined using a tracking system that measures the rover's position and orientation in the test bed at a frequency of $60\mathrm{Hz}$. The measurements from the tracking system can be used to derive the velocity and rotation rate of the rover which can then be used to derive the contact and side slip angles from the kinematics. Additionally the wheel encoders give the wheel rate measurements which are used to compute the reference wheel slip thereafter.

6.2 Choice of results and settings

1. The estimates from the EKF were not differentiable from those of the UKF for the tests presented in this chapter although there was a significant difference in estimation time. For example, the computation time on a standard office PC for the test in Section 6.5 taken by the UKF for a scenario length of $2\,\mathrm{min}$ using the *contact & side slip angle model* was $13\,\mathrm{min}$. The same scenario with the EKF took $7\,\mathrm{min}$. Here the EKF algorithm uses Jacobians (refer Section 2.5.1) computed numerically by MATLAB. Analytical Jacobians generated using the symbolic toolbox in MATLAB and fed to the estimator further reduced the estimation time to $54\,\mathrm{sec}$. Therefore all the results shown in the following sections are generated using the EKF with analytical Jacobians.

2. The filter results from the random walk and damped model of contact and side slip angles were seen to produce indistinguishable estimates for the hypothetical scenarios for a damping value of $10^{-3}\mathrm{s}^{-1}$. All the results presented in the following sections are generated using the random walk model for the contact and side slip angles.

3. For the hypothetical scenarios, the covariances for the sensor noise are calculated from previously conducted lab tests (see Table 6.1). The remaining covariances, which include those of the Euler angles, rover velocity, wheel slip, contact angles, side slip angles and the y, z components of wheel velocity in the final frame considered, are set arbitrarily to 10^{-5} (with respective units). Better results were found for wheel slip covariances set to 10^{-6} for the hypothetical scenarios.

4. For the lab scenarios, the covariances for the sensor noise is calculated during homing which is used to initialize the filter (see Table 6.1). The remaining covariances, as mentioned above, are set arbitrarily to 10^{-5} (with respective units). Better results were found for wheel slip covariances set to 10^{-7} and rover velocity covariances set to $10^{-4}\mathrm{m}^2\mathrm{s}^{-2}$ for the lab scenarios.

Table 6.1: Covariances of sensor noise

Sensor noise covariance	**FL**	**ML**	**RL**	**RR**	**MR**	**FR**
$\mathbf{n}_{q_\mathrm{s}}(\times 10^{-11}\mathrm{rad}^2)$	0	0	0	0.1298	0	0
$\mathbf{n}_{\dot{q}_\mathrm{s}}(\times 10^{-10}\mathrm{rad}^2\ \mathrm{s}^{-2})$	0	0	0	0.4767	0.3200	0
$\mathbf{n}_\mathrm{w}(\times 10^{-11}\mathrm{rad}^2\ \mathrm{s}^{-2})$	0.4313	0.4335	0	0	0.4070	0
	FL	**FR**	**R**			
$\mathbf{n}_{q_\mathrm{b}}(\times 10^{-5}\mathrm{rad}^2)$	0.1454	0.1026	0.0506			
$\mathbf{n}_{\dot{q}_\mathrm{b}}(\times 10^{-3}\mathrm{rad}^2\ \mathrm{s}^{-2})$	0.2523	0.3246	0.2431			
	x	**y**	**z**			
$\mathbf{n}_\omega(\times 10^{-4}\mathrm{rad}^2\ \mathrm{s}^{-2})$	0.3932	0.5048	0.3797			
$\mathbf{n}_f(\mathrm{m}^2\ \mathrm{s}^{-4})$	0.0013	0.0015	0.0049			

Note: A small value of 10^{-12} is added to all the covariance values to ensure non-zero values for the filter implementation. Noise terms - steering angle ($\mathbf{n}_{q_\mathrm{s}}$), steering velocity ($\mathbf{n}_{\dot{q}_\mathrm{s}}$), wheel rate ($\mathbf{n}_\mathrm{w}$), bogie angle ($\mathbf{n}_{q_\mathrm{b}}$), bogie velocity ($\mathbf{n}_{\dot{q}_\mathrm{b}}$), gyroscope ($\mathbf{n}_\omega$) and accelerometer ($\mathbf{n}_f$)

6.3 Hypothetical test for contact angle estimation

To verify contact angle estimation, a simple hypothetical scenario is considered from which the nature of the contact angles developed by the wheels can be predicted intuitively. These theoretical contact angles are then compared with those obtained from the estimator. The estimation framework for the *contact angle model* is used here.

Scenario

A hypothetical *flying* rover is considered that has one of its front bogies rotated steadily for a brief amount of time. Artificial measurements with noise properties taken from the known covariances of the real sensors onboard the ExoMars rover are generated to feed as inputs to the estimator. The front left bogie is rotated for $10\ \mathrm{s}$ at a constant rate of $0.06\ \mathrm{rad/s}$ or roughly $3\ \mathrm{deg/s}$. The rover is flying in the forward direction with a speed of $3\ \mathrm{cm/s}$. The wheel rates are calculated from the rover velocity and the wheel radius, and maintained the same for all wheels. All other measurements are taken to be zero except the gravity vector, which is taken to be pointing down with a value equal to the Earth's gravitational constant. This is also taken into account in the artificial measurements generated for the IMU's accelerometer. Fig. 6.1 shows the artificial measurements generated for the bogie angles and velocities.

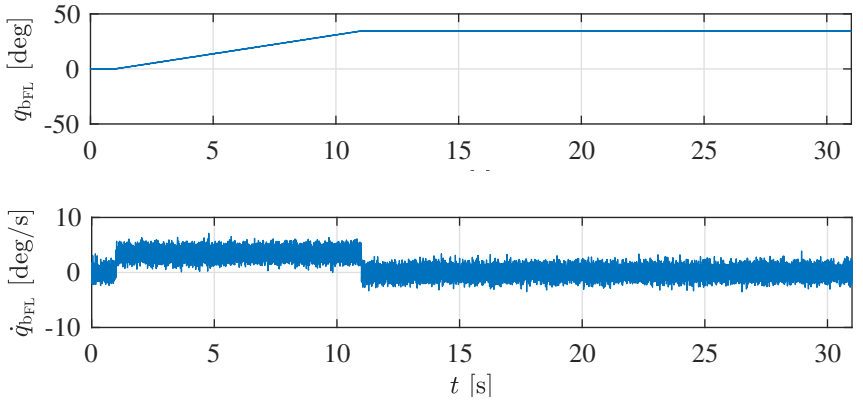

Figure 6.1: Bogie angles and velocities for FL bogie rotation scenario

The following analysis presents what the contact angles for the wheels should look like when only the front left bogie is rotated. All other bogies and steering axes are maintained at their nominal position and the rover is considered to have a purely straight forward motion. The schematic in Fig. 6.2 helps visualize the discussion below.

- The contact angles for all wheels except the ones attached to the FL bogie will be zero
- Rotation of the FL bogie leads to wheel velocity components in the xy plane of the drive frame
- Addition of the y component of the wheel velocity in drive frame contributes to contact angle
- The rotational velocity of the bogie and the forward velocity of the rover contribute to the wheel velocities and their relative magnitudes combined with the bogie angle determine the contact angles

From Fig. 6.2 it can be seen that as the bogie angle changes, the orientation of the drive frame changes along with the direction of the bogie velocity while the rover velocity direction stays the same (since the rover is assumed to have pure forward motion in the artificial measurements). This leads to a gradual decrease in the absolute value of contact angle for the FL wheel and a gradual increase for the ML wheel (Fig. 6.2 sketch (b)). Once the bogie stops rotating, the contact angle is constant and equal to the bogie angle for both wheels (Fig. 6.2 sketch (c)). The development of contact angles described above can be seen in the reference values computed from the kinematics of the rover shown in Fig. 6.3.

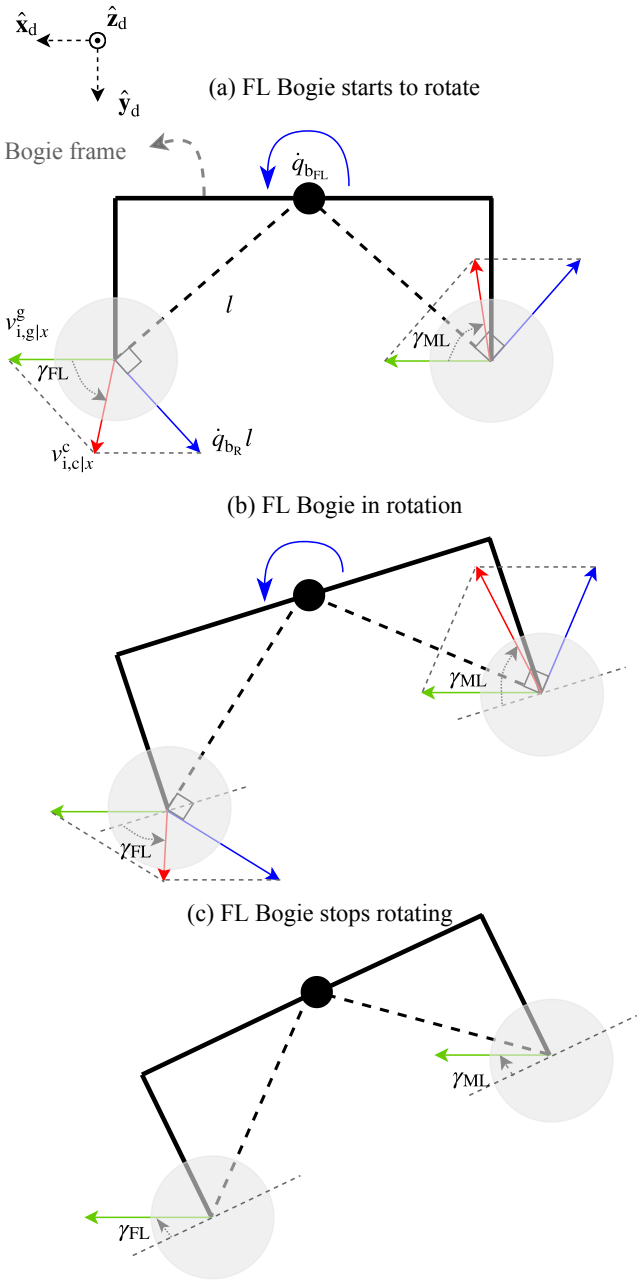

Figure 6.2: Schematic showing the development of contact angle. The schematic is drawn as seen from the left view of the rover in the xy plane of the drive frame

Filter results

Along with the reference, the estimates from the implementation of the *contact angle model* in the nonlinear Kalman filter framework are also shown in Fig. 6.3. Fig. 6.4 shows the corresponding wheel slip and rover velocity estimates. A short description of the estimates is presented below.

- The contact angles for all wheels except those attached to the FL bogie are zero as anticipated
- γ_{FL} and γ_{ML} follow the reference at the start when the bogie starts to rotate
- $v^{\mathrm{g}}_{\mathrm{i,g}|x}$ and all the six wheel slip estimates are consistently drifting away from the reference
- The absolute values of γ_{FL} and γ_{ML} are underestimated for the duration of bogie rotation
- γ_{FL} and γ_{ML} follow the reference again once the bogie stops rotating

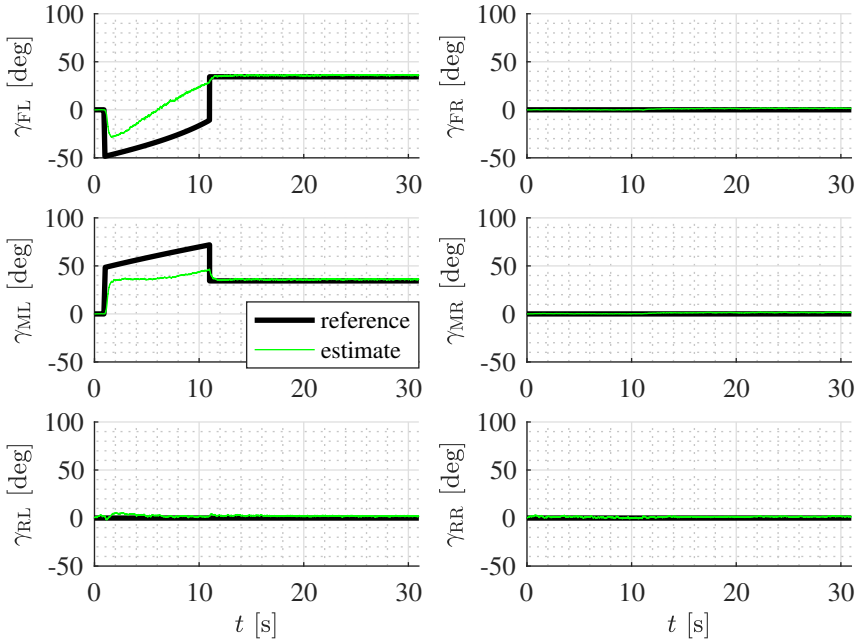

Figure 6.3: Contact angle estimates for FL bogie rotation scenario

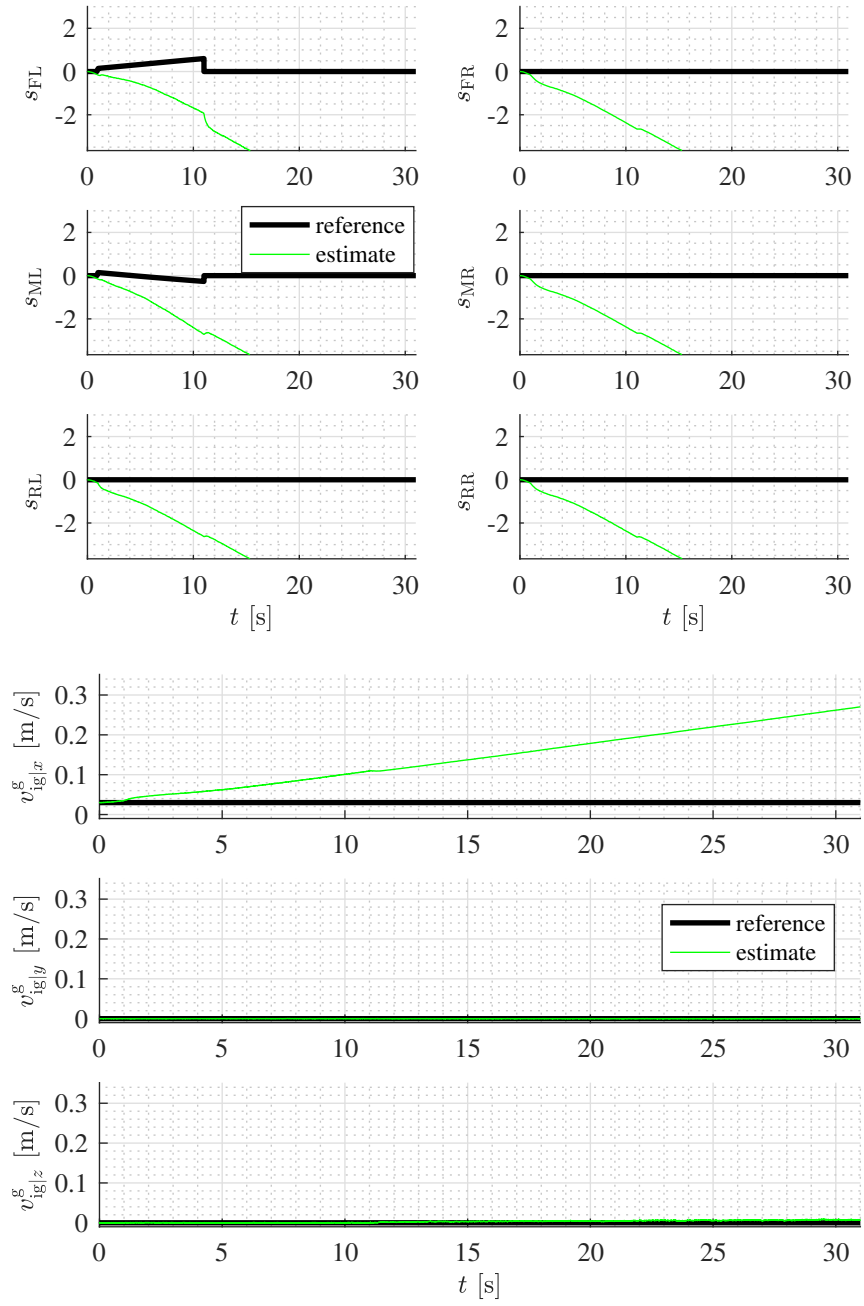

Figure 6.4: Rover velocity and wheel slip estimates for FL bogie rotation scenario

Table 6.2: RMS errors of estimates for FL bogie rotation scenario

Rover velocity^{+} (ms^{-1})		**Wheel slip*** (-)		**Contact angle*** (deg)	
O	**ND**	**O**	**ND**	**O**	**ND**
0.1361	0.0033	4.5195	0.1467	18.8466	10.8803
0.0001	0.0002	4.5199	0.1080	13.5646	10.0483
0.0042	0.0006	4.5324	0.1077	2.4683	5.5500
		4.5391	0.1033	1.3199	2.2906
		4.5435	0.1054	1.1245	0.5632
		4.5436	0.1053	1.1276	0.2298

O - errors from **o**riginal estimates. **ND** - errors from estimates where **n**on-**d**iagonal elements of $\mathbf{P_x}$ hard reset to zero. $^{+}$ - estimate errors listed in order x, y, z
* - estimate errors listed in order $\mathrm{FL}, \mathrm{ML}, \mathrm{RL}, \mathrm{RR}, \mathrm{MR}, \mathrm{FR}$

Discussion

When the rover velocity is being overestimated, revisiting the schematic in Fig. 6.2, it can be seen that if the $v^{\mathrm{g}}_{\mathrm{i,g}|x}$ component is increased, the absolute value of contact angles for both wheels decrease and this is seen in the estimation results of γ_{FL} and γ_{ML}. The rover velocity and wheel slip, although they drift a lot from the reference, are consistent with the definition of slip as detailed in Section 4.1. It can be seen that for a negative value of slip the wheel velocity corresponds to being greater than the rolling speed and hence is translated to an increase in $v^{\mathrm{g}}_{\mathrm{i,g}|x}$ estimates.

Stepping through the iterations of the filter, a closer inspection of the state error covariance matrix $\mathbf{P_x}$ (refer Section 2.5.1), revealed large values along the non-diagonal elements. This is reflected in the slip and velocity estimates as the filter is estimating large cross covariances between the contact angle states, and the wheel slip and rover velocity states. As a workaround to this problem, a hard resetting of the non-diagonal elements of the state error covariance matrix to zero was tried between the update and predict steps of the filter. The estimation results for the workaround are shown in Figs. 6.5 and 6.6. These estimates now follow the reference very closely and verify the contact angle estimation by the filter framework using the *contact angle model*. The reason for the inability of the filter model to estimate the rover velocity and wheel slip reliably is mentioned in Section 4.6.

Table 6.2 shows the Root Mean Square Errors (rmse) between the estimates and reference. The rmse of contact angle estimates for the FL and ML wheels de-

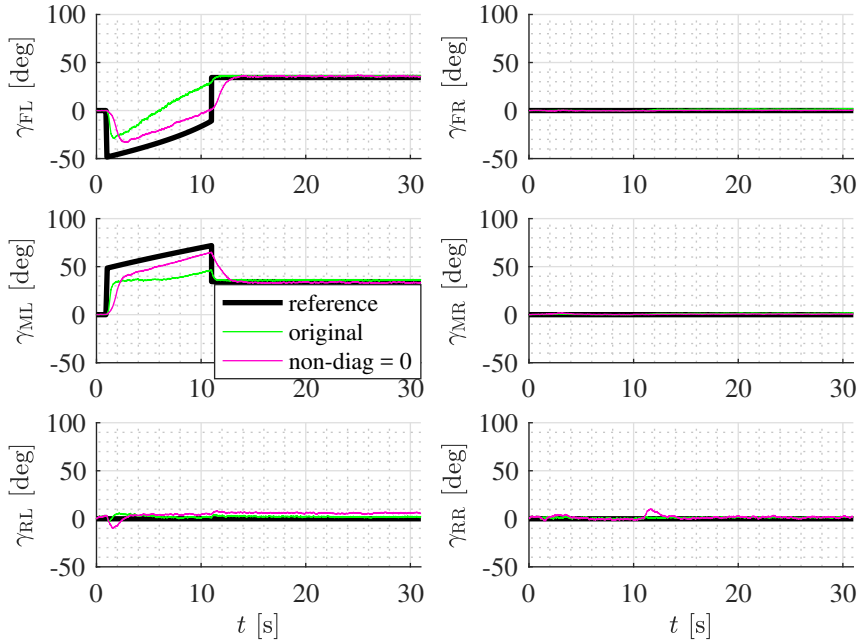

Figure 6.5: Contact angle estimates for FL bogie rotation scenario

creases by roughly $8°$ and $3°$ respectively after the hard reset of $\mathbf{P}_{\mathbf{x}}$. The rmse of $v^{\mathrm{g}}_{\mathrm{i,g}|x}$ decreases from $13.61\mathrm{cm\,s^{-1}}$ to $0.33\mathrm{cm\,s^{-1}}$. Wheel slip estimate rmse reduces on average to 0.1127 from 4.533.

6.4 Hypothetical test for side slip angle estimation

For the verification of the side slip angle estimation a hypothetical scenario is needed where the development of side slip angles is easily interpreted. The side slip angle estimation is done using the *contact & side slip angle model* built into the nonlinear Kalman filter framework.

Scenario

For the same flying rover model previously mentioned, by rotating the *rear* bogie the development of side slip angles on the two rear wheels can be predicted easily. The same parameters for bogie speed and rover velocity from Section 6.3 are used to generate artificial measurements for the rotation of the rear bogie. Similar to the analysis done for the contact angles, a consequence of rotating the rear bogie is summarized below. The schematic in Fig. 6.7 helps visualize the discussion below.

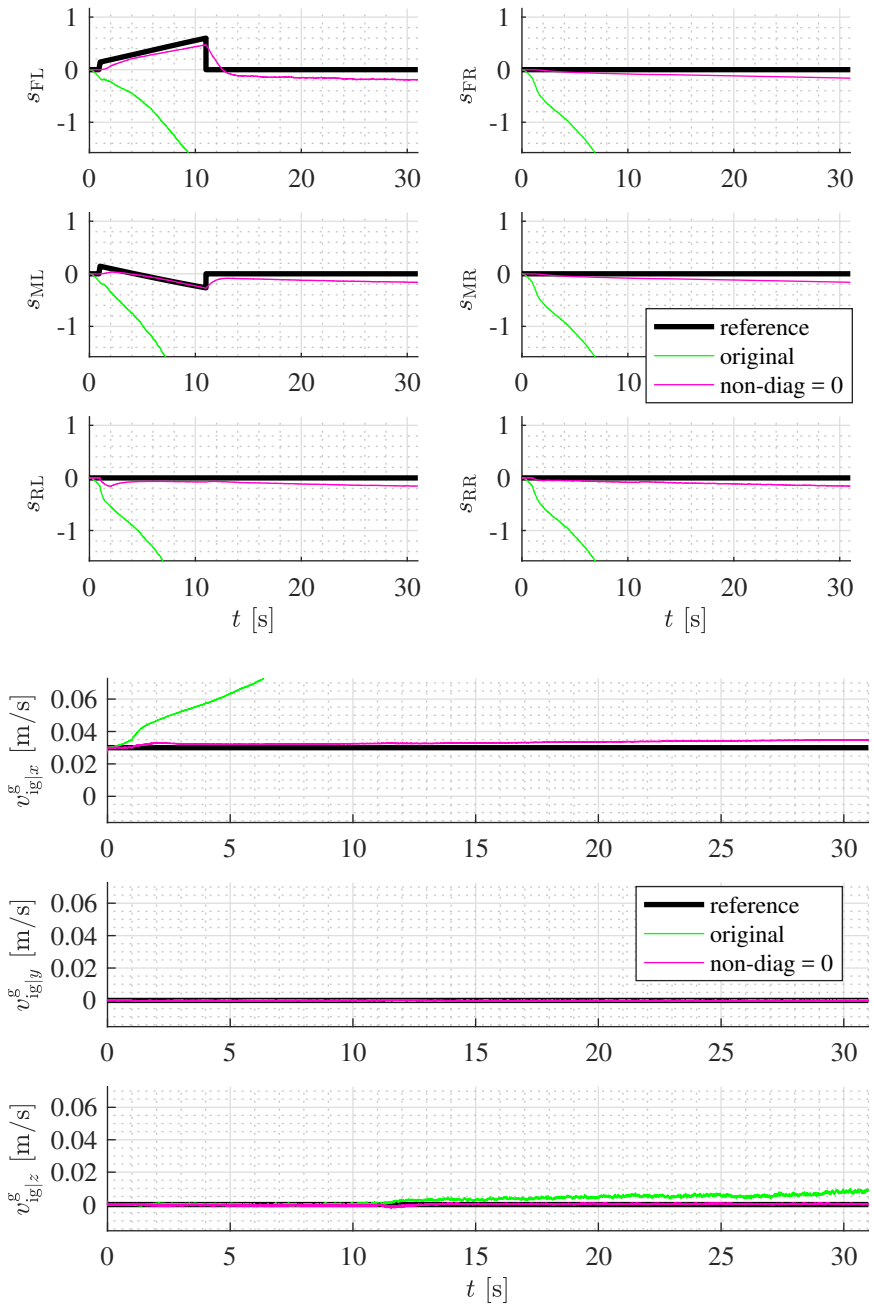

Figure 6.6: Wheel slip and rover velocity estimates for FL bogie rotation scenario

- Side slip and contact angles for all wheels except the ones attached to the rear bogie will be zero
- Rotation of the rear bogie leads to wheel velocity components in the yz plane of the drive frame
- Addition of the z component of the wheel velocity in drive frame contributes to side slip angle
- Addition of the y component of the wheel velocity in drive frame contributes to contact angle

It can be seen that as the rear bogie rotates, the orientation of the drive frame changes and with it the direction of the bogie velocity. The $v^{\mathrm{d}}_{\mathrm{i,d}|y}$ being constant throughout the bogie rotation, the contact angles γ_{RL} and γ_{RR} remain constant (Fig. 6.7 sketch (b)). Also $v^{\mathrm{c}}_{\mathrm{i,c}|y} (= v^{\mathrm{d}}_{\mathrm{i,d}|z})$ being the same at all times of the bogie rotation, the side slip angles β_{RL} and β_{RR} remain constant (Fig. 6.7 sketch (c)). It can be seen that the contact and side slip angles will be independent of the rear bogie angle.

Filter results

The development of side slip angles (and contact angles) described above can be seen in the reference values in Fig. 6.8. The estimates shown are obtained from the implementation of the *contact angle & side slip angle model* in the nonlinear Kalman filter framewor. The original estimates and those obtained by hard resetting the non-diagonal elements of $\mathbf{P_x}$ to zero are shown. Fig. 6.4 shows the corresponding wheel slip and rover velocity estimates. Table 6.3 shows the RMS errors between the estimates and reference. A short description of the estimates is presented below.

- The contact and side slip angle estimates are zero for all wheels other than the RL and RR wheels except for small spikes seen at the instant when the bogie rotation stops
- The absolute values of $\beta_{\mathrm{RL}}, \beta_{\mathrm{RR}}, \gamma_{\mathrm{RL}}$ and γ_{RR} are underestimated for the entire duration of bogie rotation in the *original* estimates and for the first $3\,\mathrm{sec}$ in the estimates from the hard reset of $\mathbf{P_x}$
- $v^{\mathrm{g}}_{\mathrm{i,g}|x}$ and all the six wheel slip estimates are consistently drifting away from the reference for the *original* estimates
- Overall filter estimates improve when the non-diagonal elements of $\mathbf{P_x}$ are hard reset to zero

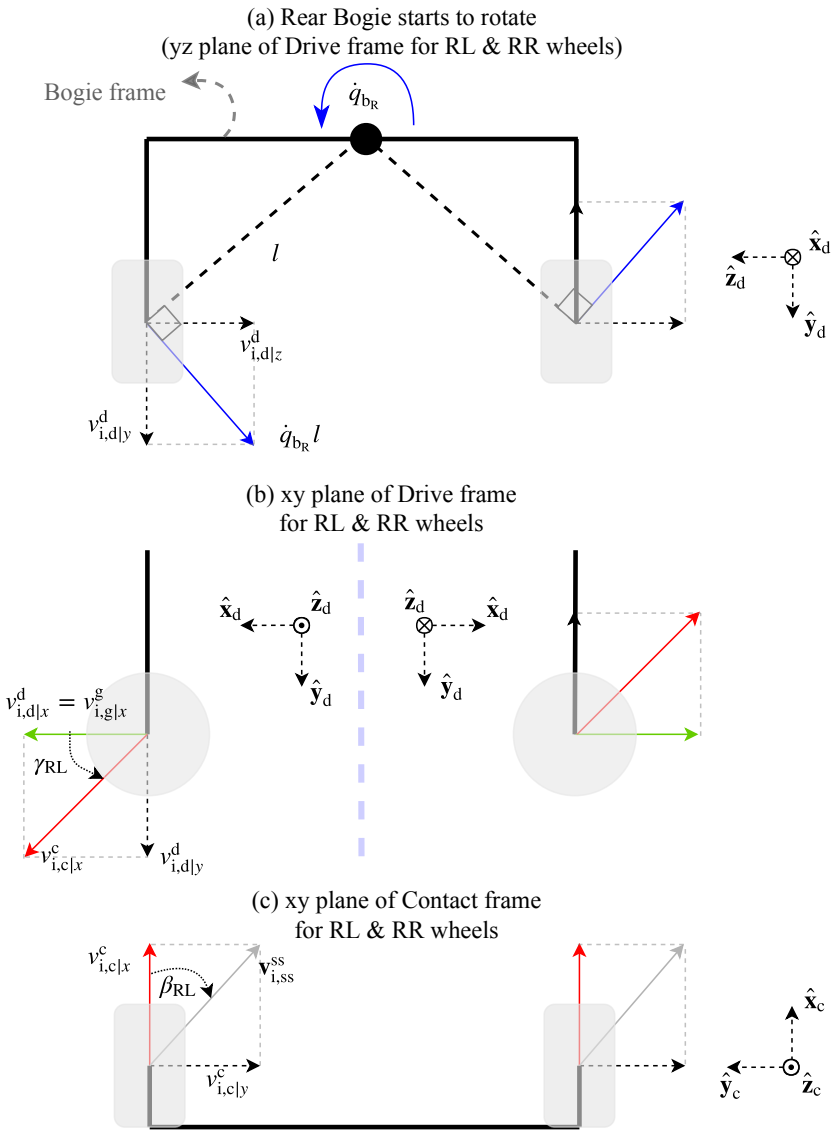

Figure 6.7: Schematic showing the development of contact angle. The schematic is drawn as seen from the left view of the rover in the xy plane of the drive frame

Discussion

In the *original* estimates as the filter overestimates $v^g_{i,g|x}$, the absolute values of γ_{RL} and γ_{RR} decrease (refer Fig. 6.7 sketch (b)) which results in increase of the respective $v^c_{i,c|x}$. As the $v^c_{i,c|x}$ increases, the absolute value of β_{RL} and β_{RR} de-

Table 6.3: RMS errors of estimates for Rear bogie rotation scenario

Rover velocity^{+} (ms^{-1})		**Wheel slip*** (-)		**Contact angle*** (deg)		**Side slip angle*** (deg)	
O	**ND**	**O**	**ND**	**O**	**ND**	**O**	**ND**
0.1248	0.0019	4.1605	0.0542	0.1166	0.4809	0.5788	1.1080
0.0015	0.0005	4.1605	0.0541	0.1256	0.2222	0.6385	0.6931
0.0003	0.0002	4.1286	0.1461	14.2250	10.1665	4.7350	3.2424
		4.1332	0.1507	14.2221	8.2933	4.8228	3.4059
		4.1589	0.0672	0.2172	0.9909	0.6177	0.7210
		4.1589	0.0672	0.1395	0.5518	0.5966	0.9403

O - errors from **o**riginal estimates. **ND** - errors from estimates where **n**on-**d**iagonal elements of $\mathbf{P_x}$ hard reset to zero. $^{+}$ - estimate errors listed in order x, y, z
* - estimate errors listed in order $\mathrm{FL}, \mathrm{ML}, \mathrm{RL}, \mathrm{RR}, \mathrm{MR}, \mathrm{FR}$

crease (refer Fig. 6.7 sketch (c)). These are reflected in the underestimated values of $\beta_{\mathrm{RL}}, \beta_{\mathrm{RR}}, \gamma_{\mathrm{RL}}$ and γ_{RR}. The relation between the drift in $v^{\mathrm{g}}_{\mathrm{i,g}|x}$ and wheel slips is the same as seen in the previous section and likewise the filter estimates are improved by hard resetting the non-diagonal elements of the state error covariance matrix to zero. The results then follow the reference very closely.

The rmse in the side slip angle estimates for the rear wheels reduce by roughly $1.4°$ (refer Table 6.3) after the hard reset of $\mathbf{P_x}$. The rmse in contact angle estimates of the RL and RR wheels reduce by roughly $4°$ and $6°$ respectively. The improvement in the rmse of wheel slip and rover velocity estimates is similar to the results from the FL bogie rotation scenario. The estimates obtained after the hard-reset of $\mathbf{P_x}$ are therefore in fairly good agreement with the reference and thus verifies the side slip angle estimation by the filter framework using the *contact & side slip angle model*.

6.5 Lab test for contact angle estimation

The estimation of contact angles has so far been verified only with a hypothetical scenario. Now a real scenario from a test conducted in the PEL lab at DLR is fed to the estimator.

Scenario

A test was performed by driving the right side of the rover over an obstacle and the measurements from the sensors fed to the estimator. Fig. 6.10 shows the FR wheel

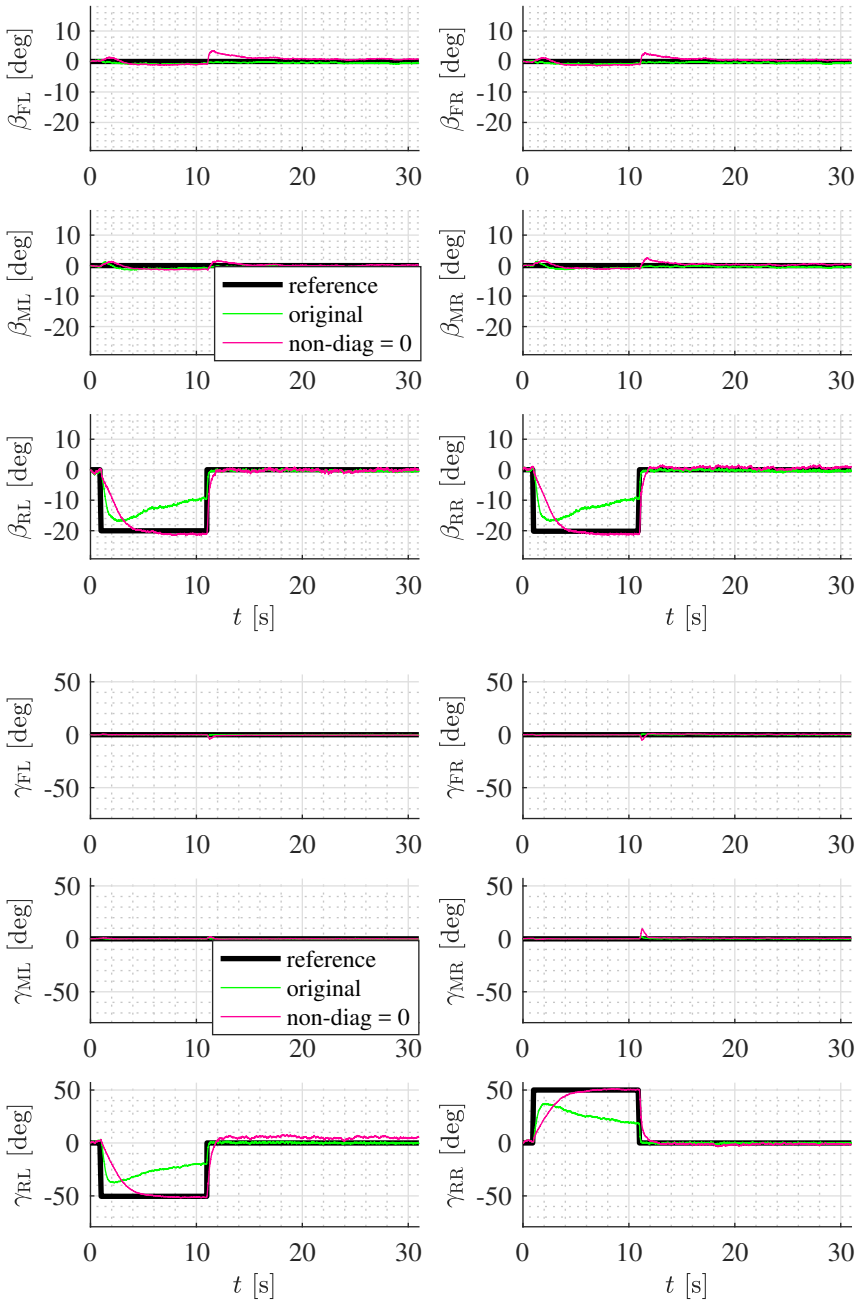

Figure 6.8: Side slip angles and contact angle estimates for Rear bogie rotation scenario

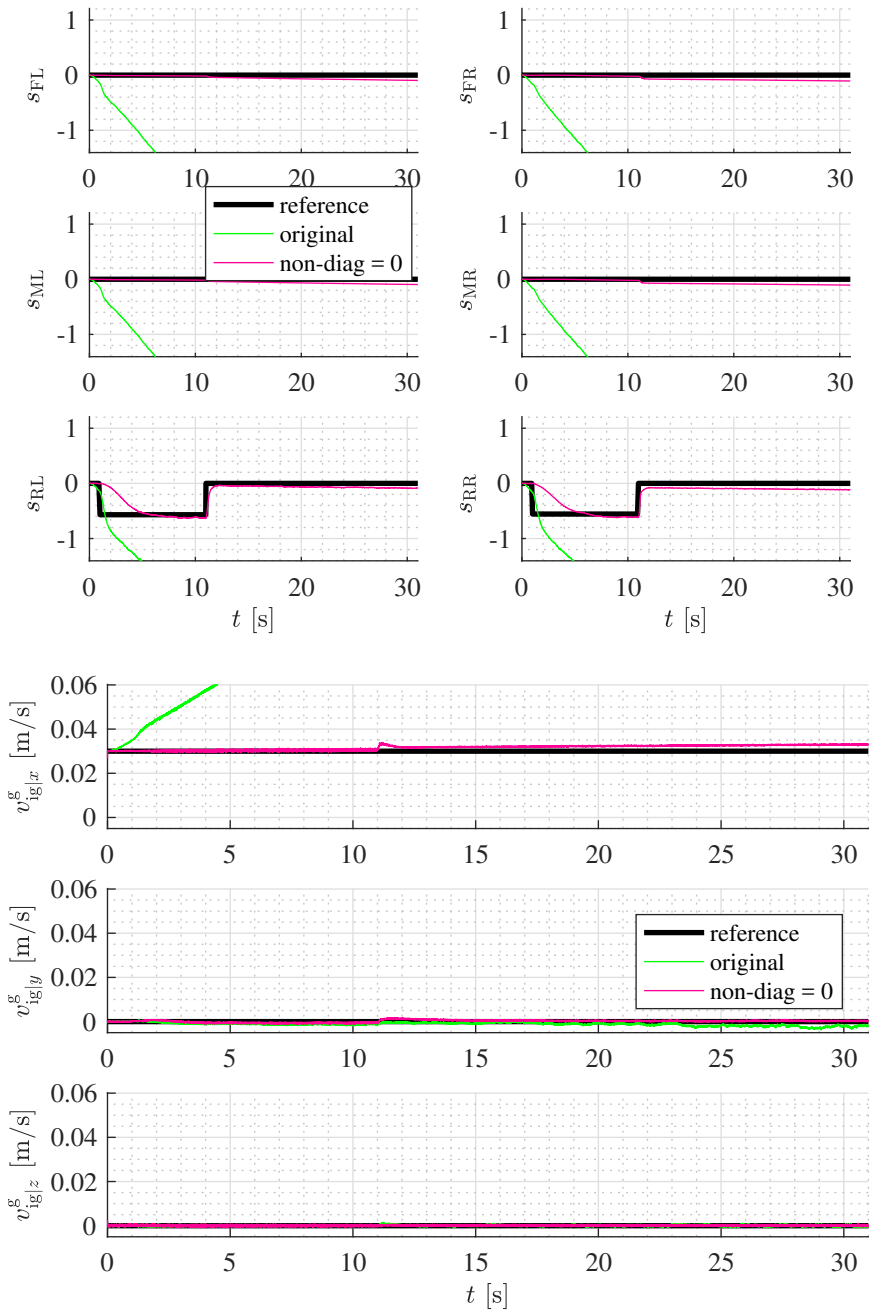

Figure 6.9: Wheel slip and rover velocity estimates for Rear bogie rotation scenario

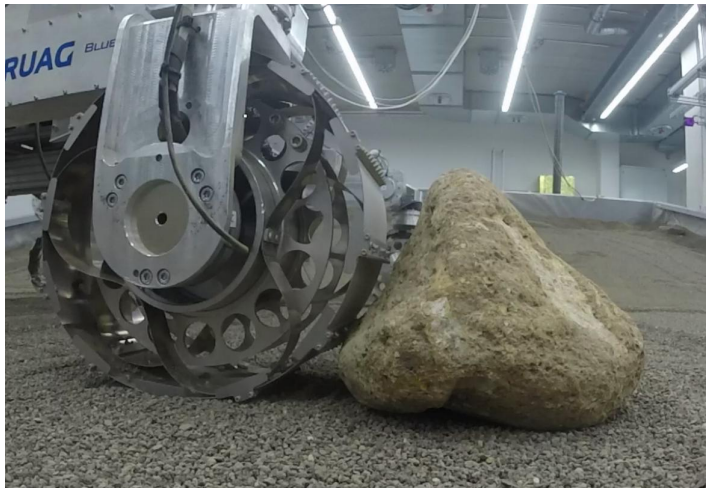

Figure 6.10: FR wheel climbing obstacle. Courtesy DLR.

of the rover climbing over the obstacle at the PEL. A time series of events of the test scenario is summarized in Fig. 6.11 along with the reference contact angles for the scenario. A quick overview of how the contact angles are developed is given below.

- When the rover is stationary, the contact angle is undefined. A non-zero constant value is seen in the reference in Fig. 6.11. This is because the reference is generated so as to maintain the previous value of contact angle in cases of singularity. Therefore this large value is a result of noisy tracking measurement leading to an erroneous contact angle that is maintained for the period that the rover stands still.

- As the rover starts to drive and the FR wheel touches the obstacle, its contact angle grows initially and then starts decreasing as the bogie joint passively starts to comply with the shape of the obstacle

- In this time the absolute value of contact angle on the MR wheel increases as the bogie angle increases

- When the FR wheel rolls over the peak of the obstacle the contact angle crosses from a positive to negative value and increases briefly until the bogie angle starts to decrease again, after which the contact angle drops to zero.

- In this time the contact angle on the MR wheel drops to zero as the bogie angle comes back to zero.

- The contact angle developed on the MR and RR wheels while climbing the obstacle can be understood in a similar way
- The climbing of RR wheel on the obstacle also leads to small contact angles on the FR and MR wheels because of small pitch angles developed by the rover.

Filter results & discussion

The estimation for this scenario was carried out using both the *contact angle model* and the *contact & side slip angle model* built into the estimator framework. For the sake of brevity in the discussion that follows the two models shall be referred to as model **C** and model **C+SS** respectively. Figs. 6.12 and 6.13 show the estimation results along with the reference. Table 6.4 shows the RMS errors between the estimates and reference for both models. Note that the RMS errors are calculated only for estimates of the rover when it is in motion.

Table 6.4: RMS errors of estimates for wheels climbing obstacle scenario

Rover velocity^{+} (ms^{-1})		**Wheel slip*** (-)		**Contact angle*** (deg)		**Side slip*** **angle**(deg)
C	**C+SS**	**C**	**C+SS**	**C**	**C+SS**	**C+SS**
0.0062	0.0037	0.2573	0.1300	8.5180	9.4303	21.5050
0.0015	0.2196	0.0134	0.1062	8.5517	9.9061	20.0045
0.0044	0.1994	0.0041	0.1014	7.9867	9.4233	38.0807
		0.1602	0.1155	13.9642	13.6912	64.8442
		0.1805	0.1308	14.2626	16.7634	19.4695
		0.1950	0.1715	13.1198	15.3854	21.9920

C - errors from *contact angle model*. **C+SS** - errors from *contact & side slip angle model*. $^{+}$ - estimate errors listed in order x, y, z. * - estimate errors listed in order $\mathrm{FL}, \mathrm{ML}, \mathrm{RL}, \mathrm{RR}, \mathrm{MR}, \mathrm{FR}$

Contact angles: Between $t = 0$ and $t = 18$ sec estimates do not follow reference. This is the period where the rover is stationary (case of singularity). Estimates follow reference with a slight lag for all wheels that are climbing the obstacle. From $t = 108$ sec to end of scenario, estimates deviate from reference. $t = 108$ sec is the instant when the RR wheel climbs off the obstacle and there are huge vibrations induced on the rover which were manifest in the spikes observed in all sensor measurements. The average rmse of contact angle estimates, excluding regions of singularity, is 11.0672° for model **C** and 12.4422° for model **C+SS**.

Time (sec)	**Description**
$t = 0$	Rover stationary
$t = 18$	All wheels straight; starts
$t = 35$	FR wheel climbs obstacle
$t = 45$	FR wheel at obstacle peak
$t = 55$	FR wheel off obstacle
$t = 60$	MR wheel climbs obstacle
$t = 70$	MR wheel at obstacle peak
$t = 80$	MR wheel off obstacle
$t = 90$	RR wheel climbs obstacle
$t = 100$	RR wheel at obstacle peak
$t = 108$	RR wheel off obstacle
$t = 112$	Rover stops

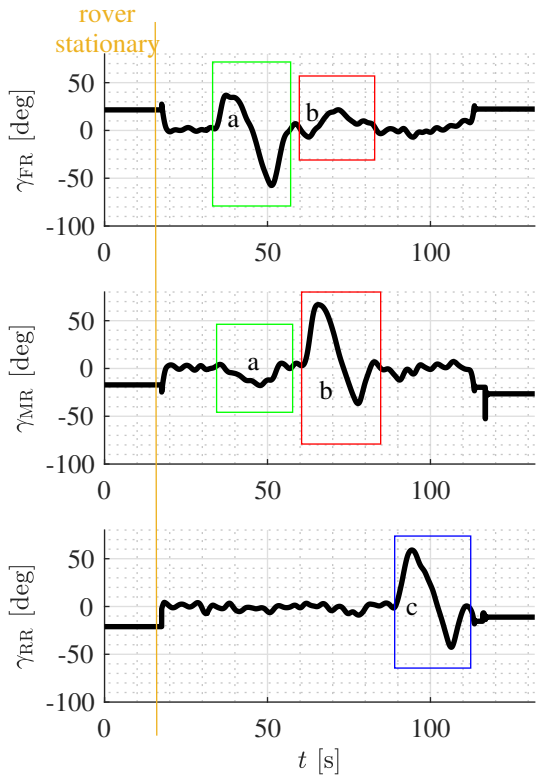

Figure 6.11: Lab test: Right wheels of rover climbing obstacle
Reference contact angles for (a) FR wheel (b) MR wheel (c) RR wheel climbing obstacle

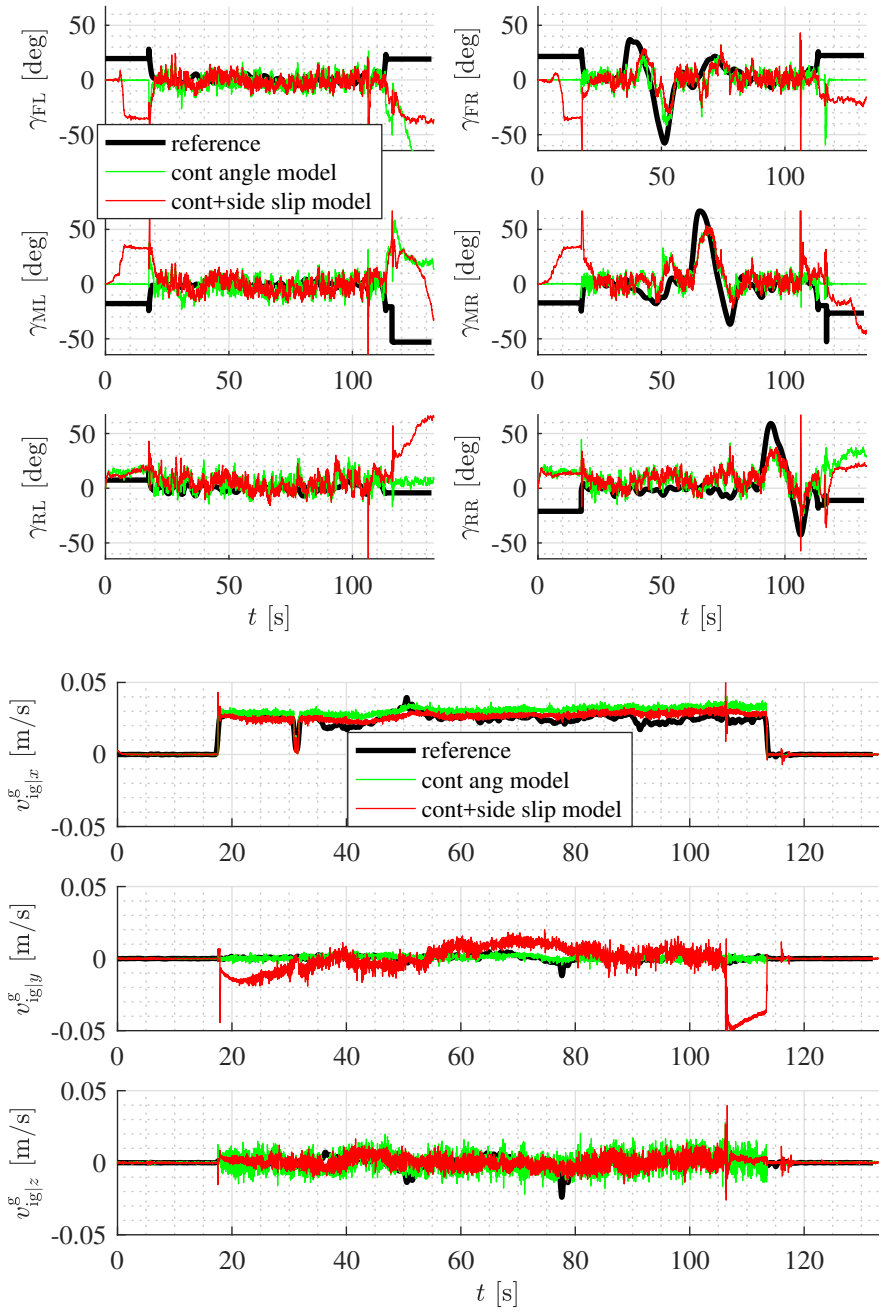

Figure 6.12: Contact angles and rover velocity estimates for wheels climbing obstacle scenario

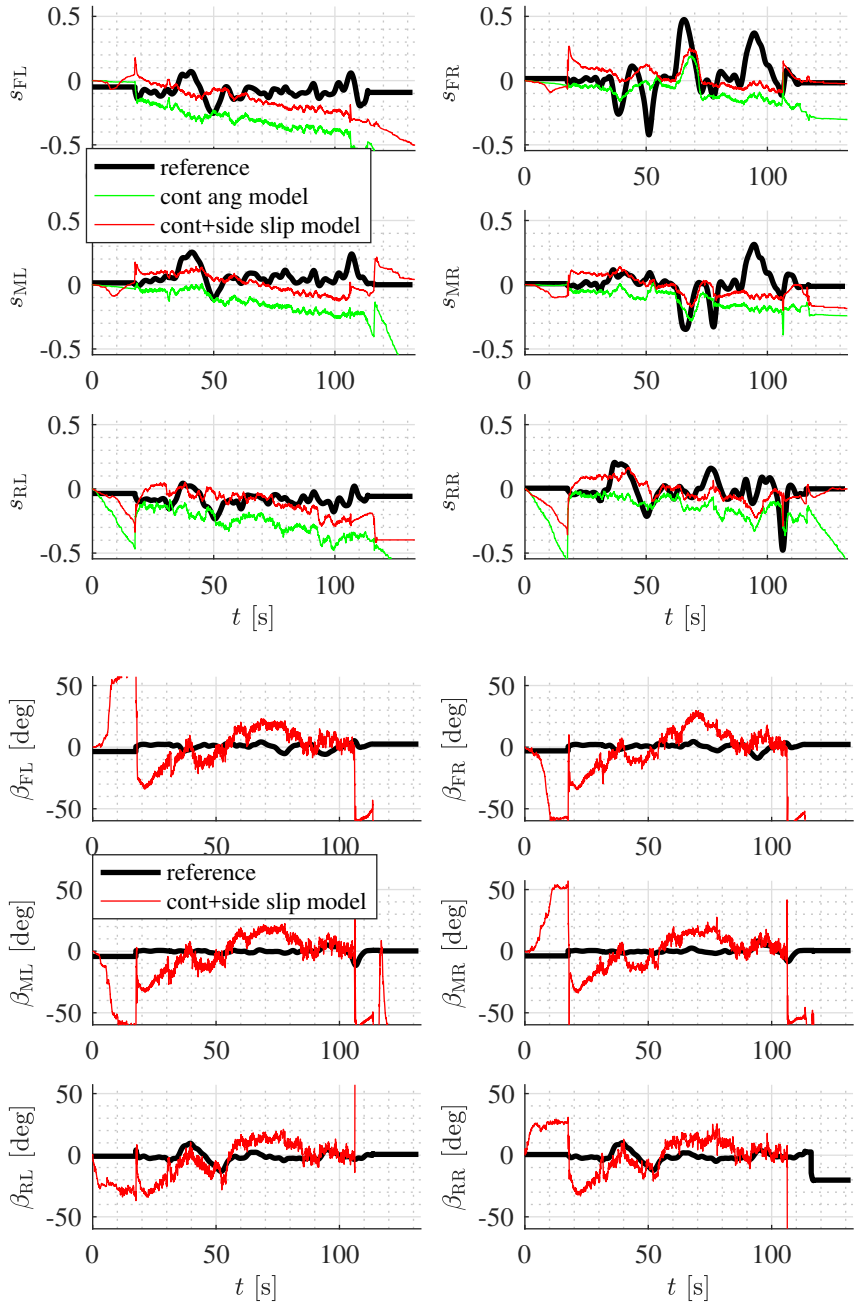

Figure 6.13: Wheel slip and side slip angle estimates for wheels climbing obstacle scenario

Rover velocity: Between $t = 18$ and $t = 112$ sec, the rover is in motion except at $t = 32$ sec where a short stop was made before driving the rover over the obstacle. At the start of motion and at the instant when the RR wheel climbs off the obstacle and induces large vibrations, the estimates show some spikes. For both models, the $v^{\mathrm{g}}_{\mathrm{i,g}|x}$ estimates are marginally overestimated. With model **C+SS** the $v^{\mathrm{g}}_{\mathrm{i,g}|x}$ estimates improve but $v^{\mathrm{g}}_{\mathrm{i,g}|y}$ estimates deteriorate. $v^{\mathrm{g}}_{\mathrm{i,g}|y}$ estimates from model **C+SS** take a while to stabilize at the start of motion. Errors in $v^{\mathrm{g}}_{\mathrm{i,g}|y}$, $v^{\mathrm{g}}_{\mathrm{i,g}|z}$ estimates from model **C+SS** are seen to increase by 2 orders of magnitude (refer Table 6.4). After the MR wheel climbs off the obstacle between $t = 60$ and $t = 80$ sec, they deviate significantly.

Wheel slip: Between $t = 0$ and $t = 18$ sec estimates deviate from reference. This is the period where the rover is stationary (case of singularity). The remainder of the estimates show some similarity in trend with the reference, however the estimates lag and drift steadily over time. As the slip estimates drift, the $v^{\mathrm{g}}_{\mathrm{i,g}|x}$ estimates are overestimated. The wheel slip estimates from model **C+SS** are seen to improve over those from model **C** for the right wheels.

Side slip angle: As with the other estimates, when the rover is stationary (case of singularity) and when the RL wheel climbs off obstacle, the estimates deviate greatly from reference. The deviation in side slip angle estimates between $t = 18$ and $t = 30$ sec are consistent with the deviation seen in the $v^{\mathrm{g}}_{\mathrm{i,g}|y}$ estimates. Between $t = 35$ and $t = 55$ sec which is when the FR wheel climbs over the obstacle, the estimates for the rear wheels are in good agreement with the reference. For the duration of the MR and RR wheels climbing over the obstacle the estimates predict a *leftward* lateral wheel velocity which is seen in the positive values of $v^{\mathrm{g}}_{\mathrm{i,g}|y}$ being estimated. The overall side slip angle estimates have huge variations with an average rmse of 30.9827°.

6.6 Lab test for side slip angle estimation

In order to verify side slip angle estimation with a real scenario, a lab test was performed to induce side slip of the wheels of the rover.

Scenario

The FL wheel of the rover was steered incrementally while maintaining all other wheels at zero steering angles. A time series of events describing the test scenario is shown in Section 6.6. The test was performed such that the steering of one wheel different from the other parallel wheels did not cause the rover to turn significantly.

Therefore the rover continued to travel almost in a straight line. The analysis of how the side slip angles develop for this test scenario is described below.

- The steering of the wheel adds wheel velocity components in the xz plane of the drive frame
- Recall that a *leftward* lateral wheel velocity in the drive frame as seen from the top view leads to a positive side slip angle
- Since the FL wheel is steered *leftward* the rover velocity in the rotated drive frame is now manifest as a rightward lateral wheel velocity and therefore a negative side slip angle is developed
- Since the rover essentially travels in a straight line when the FL wheel is steered incrementally, the side slip angle is nearly equal in magnitude to the steering angle (refer Fig. 6.14).

Time (sec)	**Description**
$t = 0$	Rover stationary
$t = 4$	All wheels straight; starts (backwards)
$t = 25$	FL wheel steered to $+10°$
$t = 38$	FL wheel steered to $+20°$
$t = 53$	FL wheel steered to $+30°$

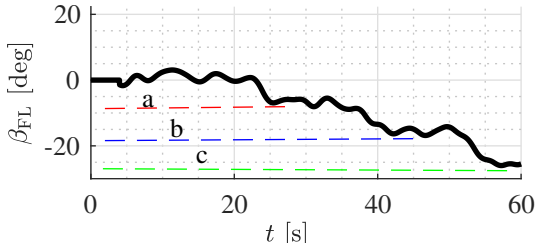

Figure 6.14: Lab test: FL wheel of rover steered incrementally
FL wheel steered to (a) $10°$ (b) $20°$ (c) $30°$

Filter results & discussion

Fig. 6.13 shows the estimation results along with the reference. Table 6.5 shows the RMS errors between the estimates and reference. Note that the RMS errors are calculated only for estimates of the rover when it is in motion.

Table 6.5: RMS errors of estimates for FL wheel incrementally steered scenario

Rover velocity^{+} (ms^{-1})	**Wheel slip*** (-)	**Contact angle*** (deg)	**Side slip angle*** (deg)
0.0018	0.0784	6.6249	4.2948
0.0023	0.0746	6.6725	4.4154
0.0024	0.0528	6.6132	4.7044
	0.0357	6.3794	4.4368
	0.0460	7.1936	4.2025
	0.0455	6.5520	4.4611

$^{+}$ - estimate errors listed in order x, y, z

* - estimate errors listed in order $\mathrm{FL}, \mathrm{ML}, \mathrm{RL}, \mathrm{RR}, \mathrm{MR}, \mathrm{FR}$

Side slip angle: Between $t = 0$ and $t = 4$ sec, the estimates deviate from reference. This is the region of singularity since the rover is stationary. The side slip angles between $t = 4$ and $t = 12$ sec are overestimated. β_{FL} follows the reference well, showing the side slip induced by the incrementally steered wheel. Between $t = 30$ and $t = 40$ sec, the estimates deviate slightly from reference. The rmse of estimates is on average $4.4192°$.

Rover velocity: $v^{\mathrm{g}}_{\mathrm{i,g}|x}$ estimates follow reference closely till about $t = 50$ sec, after which it drifts slightly. Between $t = 8$ and $t = 12$ sec, $v^{\mathrm{g}}_{\mathrm{i,g}|y}$ deviates from reference and this is reflected in the overestimation of side slip angles mentioned previously. Between $t = 30$ and $t = 40$ sec, the deviation in estimates from the reference is consistent with the drift in the corresponding side slip angles. The estimates of y, z components of the rover velocity are a bit noisy compared to the estimates of x component, subsequently, their rmse are slightly larger.

Wheel slip: From around $t = 20$ sec for the front and middle wheels, and $t = 40$ sec for the rear wheels, the wheel slip estimates drift from the reference. The deviations are consistent with those seen in the $v^{\mathrm{g}}_{\mathrm{i,g}|x}$ estimates. The average rmse of the estimates is 0.0557.

Contact angles: The first $t = 4$ sec is the period when the rover is stationary and therefore the contact angle is not defined. The variation in the estimates for the remainder of the scenario appear largely random with a mean roughly equal to zero. The rmse is equal to $6.6726°$ on average.

The estimates from the filter built on *contact & side slip angle model* were seen

to be poor for the side slip estimates in the scenario of the rover climbing over the obstacle. In contrast the estimates of side slip angles in the scenario of individual wheel steer show good adherence to the reference values. Therefore it appears that the estimator is unable to estimate both the side slip and contact angle reliably for the case of non-zero contact angles like in the obstacle scenario. Also the steering of the single wheel largely induced side slip in that particular wheel alone, therefore this is a more simple scenario with less dynamics as compared to the obstacle scenario.

An oscillation in cross-coupling of states was seen in the estimates of $\mathbf{P_x}$ between the predict and correct steps of the filter. The predict step produced non-zero cross covariances in the Euler angles and rover velocity states, and the correct step lead to cross-covariances for all states excluding the Euler angles. Upon hard resetting the non-diagonal elements of $\mathbf{P_x}$ to zero between the correct and predict step the filter estimates largely improved.

This chapter presented scenarios that focused on contact and side slip angle estimation. The results show the feasibility of estimating the wheel-terrain contact angles and additionally side slip angles for uneven terrain using the extension of the estimation framework for rover velocity and wheel slip. Several challenges to obtaining good results for all the states without compromising one or the other are seen. Certain estimates are not understood clearly and require further work to ascertain the nature of estimation given the complexities of the system. The following chapter concludes the thesis work and suggests scope for future work.

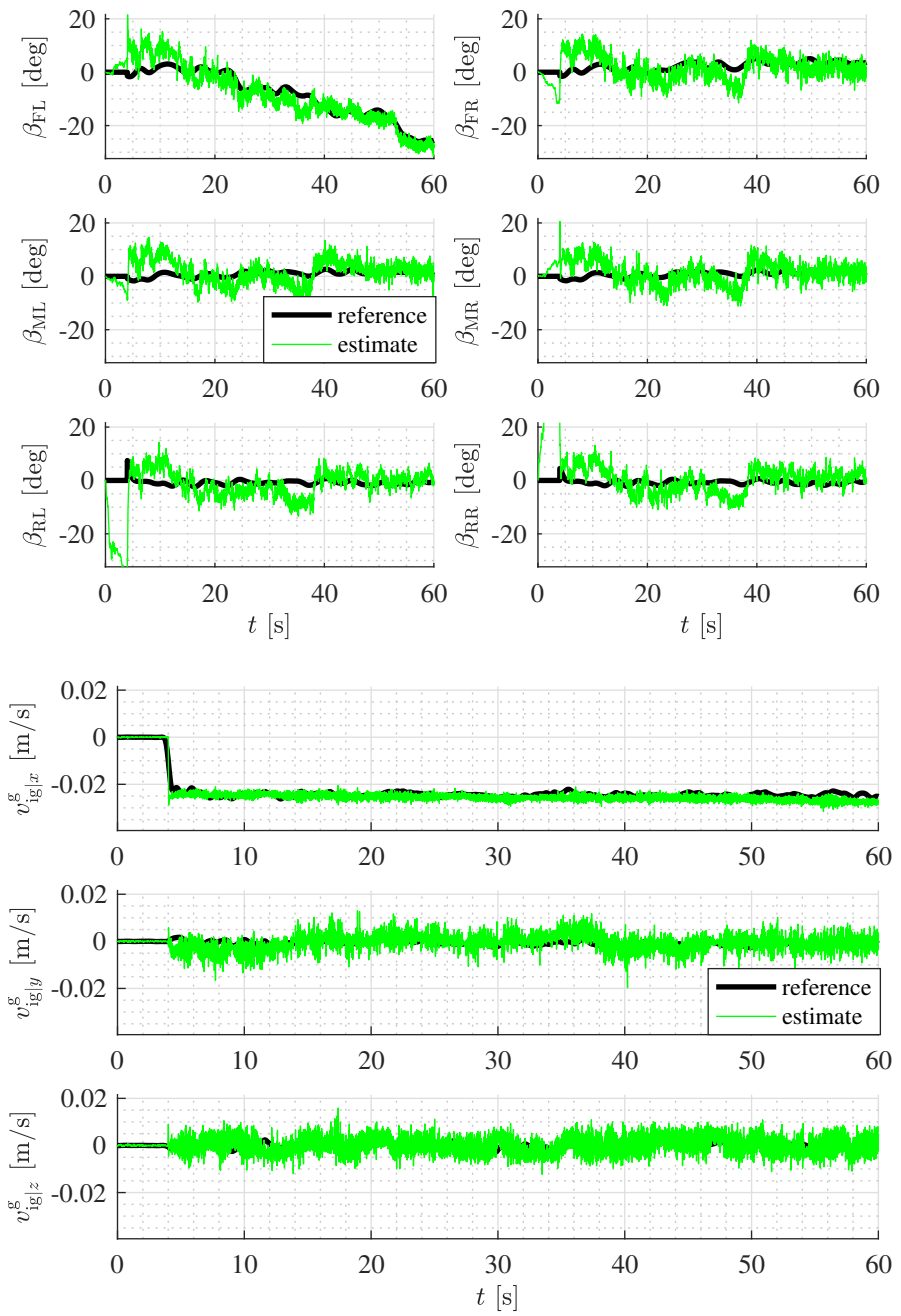

Figure 6.15: Side slip angle and rover velocity estimates for FL wheel incrementally steered scenario

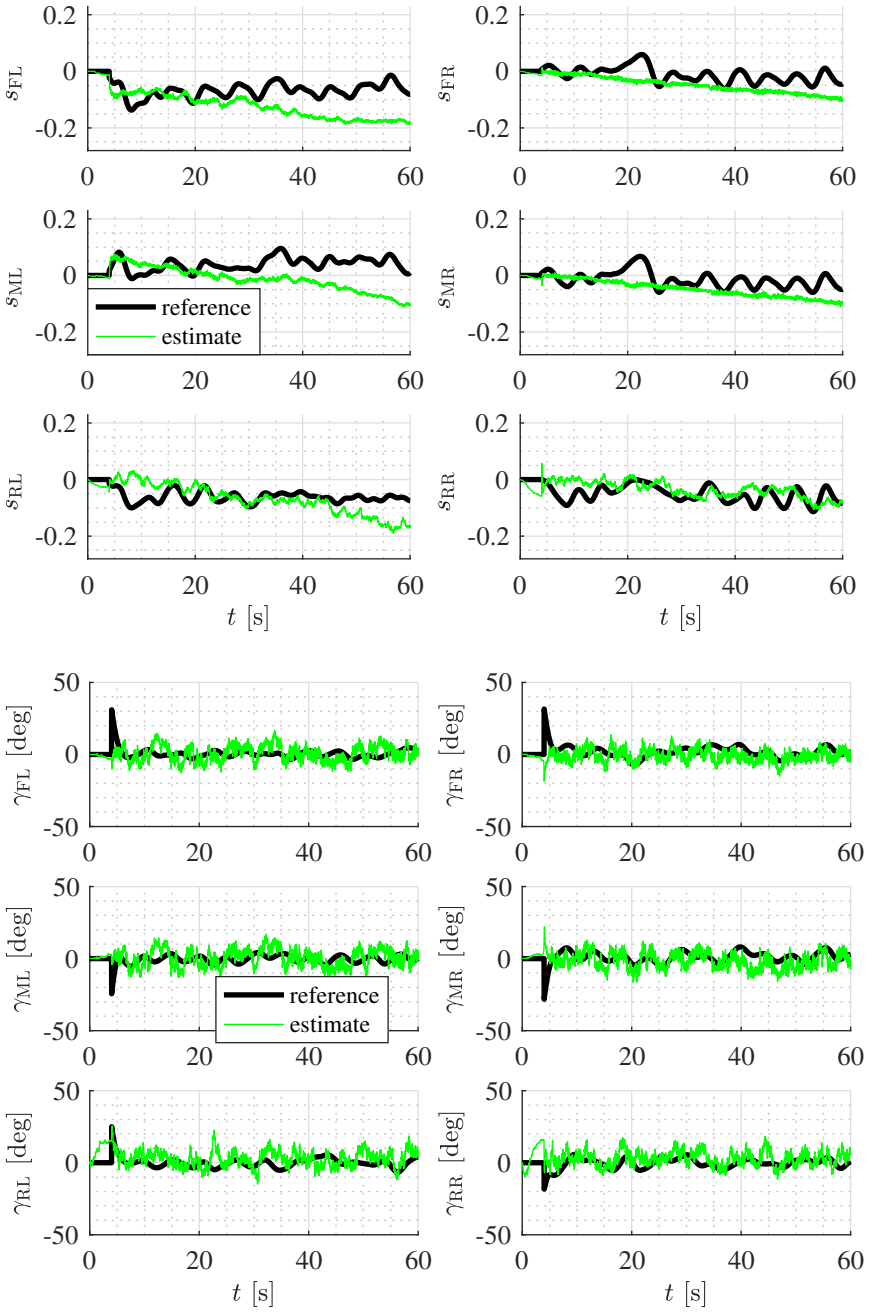

Figure 6.16: Wheel slip and contact angles estimates for FL wheel incrementally steered scenario

Chapter 7

Conclusions and Future Work

7.1 Conclusion

The determination of motion states of a rover while travelling on uneven terrain is a challenging task. The goal of the research was to be able to estimate the motion states of the rover using the 3D differential kinematics and sensor fusion from relatively inexpensive sensors onboard like the IMU, potentiometers and wheel encoders. This thesis thereby presented an approach to achieving this goal without the use of additional sensors or terrain knowledge.

The existing framework described in Chapter 4 was capable of capturing the motion states of a rover only while driving on smooth terrain which assumed purely longitudinal motion of wheels. The motion states estimated were the rover velocity and wheel slip. In Chapter 5 the introduction of a wheel-terrain contact angle was proposed to account for vertical motion of wheels on uneven terrain. A side slip angle was also introduced to account for possible lateral motion of wheels. The 3D differential kinematics of the rover were extended to include the contact and side slip angles. In the absence of knowledge of the terrain, the dynamic behaviour of contact and side slip angle states were modelled as a *random walk*. The 3D differential kinematics and contact and side slip angle states were added to the existing framework of estimation by modifying a standard strapdown algorithm. A nonlinear Kalman filter was used for the combined estimation of rover velocity, wheel slip, contact angle and side slip angle.

In Chapter 6 the filter framework developed was verified for contact angle and side slip angle estimates against hypothetical scenarios and tests conducted at the PEL, DLR.

The initial results from the filter presented problems with the state error covariances estimated. Large cross covariances of the states estimates deteriorated the results. As a workaround to this problem the cross covariances of the state error covariance estimates were hard reset to zero in each iteration of the filter. Subsequently the estimates were found to be in good agreement with the reference values with a few difficulties like drift in rover velocity and wheel estimates still persisting. The estimates in general showed poor adherence to the reference in cases of singularities i.e. when the rover was motionless. The contact angle estimates from the filter framework built upon the *contact angle model* for a scenario of one side of the rover climbing over an obstacle had a RMS error on average of 11.0672 degrees on average. The contact angle estimates from filter built upon the *contact & side slip angle* for the same scenario had a RMS error of 12.4422 degrees on average. However the estimates of the side slip angles were seen to be quite unreliable which was reflected in the deterioration of lateral velocity estimates of the rover.

The side slip angle estimates for a scenario of incrementally steering an individual wheel had an average RMS error of 4.4192 degrees. Therefore the *contact & side slip angle mode* is able to handle the estimation of side slip angle for an individual wheel experiencing side slip well. However it is unable to produce good estimates for the case when there are non-zero contact angles for several wheels as in a scenario with one side of the rover climbing over an obstacle.

With regard to the nonlinear Kalman filter performance, the estimation of motion states using the EKF were indistinguishable from those using the UKF, but with a significantly shorter computation time. Therefore the linearization of state transition and measurement functions done in the EKF algorithm was seen to be capable of handling the nonlinearities of the system discussed in Section 5.7.

7.2 Future work

The development of the wheel-terrain contact angle estimation in this thesis forms a basis for the concept verification and demonstration of the feasibility of estimating the contact angles from minimal sensors and simple kinematic modelling of the rover. Future improvements could include making the filter capable of handling the singularities associated with the definition of wheel slip, contact angle and side slip angle. The limitations of the measurement model discussed in Section 4.6 could also be addressed in future work.

The covariances used to describe the uncertainties in the system modelling could be optimized for better filter results. An analytical technique to compute the initialization of state error covariance matrix based on the covariances of the system states is presented in (Kneip et al., 2010). This could be implemented along with the aforementioned optimization of state covariances.

More rigorous testing of the filter estimation capabilities need to be performed with different scenarios. A study on the limiting cases, if any, could be done to determine under what operating conditions the EKF algorithm may lead to divergent results for the linearization of the system.

The reason for the large cross coupling of states estimated by the filter algorithm could be investigated. This may reveal a deeper understanding of the physical dynamics of the system, apart from numerical errors in the computation of the state error covariance matrix.

The system response may be studied for longer durations of bogie rotations in the hypothetical scenarios presented in Chapter 6. It would be interesting to see if the contact and side slip angle estimates reach a steady state error or if the errors grow continually. The results from the hard resetting of $\mathbf{P_x}$ also appear to have the characteristics of a second-order linear system with a longer settling time and zero steady-state error. Whereas the original estimates seem to have a shorter settling time with an overshoot and steady-state error. With the hard resetting of $\mathbf{P_x}$, the system appears to behave as if an integrator were added to the system model. This could be further studied.

The analysis of the results may suffer from inadequacies due to the nature in which the references were calculated. Therefore the RMS errors indicated in the discussion of results are not the final truth. Better techniques to more reliably develop an accurate reference could be developed to provide a more credible comparison between the true and estimated states of the rover.

Possible areas of interest could also be in the comparison of random walk and damped models for the modelling of contact and side slip angles to identify cases when one might be better than the other. Furthermore the influence of the value of damping parameter chosen could be investigated. Alternatively a different approach to modelling the dynamic behaviour of contact and side slip angle could be researched.

The filter framework is currently coded in MATLAB. The generation of C code for the nonlinear Kalman filter estimation could be done to speed up the estimation process and give it real-time capabilities. The online estimation of the motion states is the next step to making the estimates of the contact and side slip angles useful for real-time decision-making and control.

To reduce the gradual drift in the rover velocity and wheel slip estimates, an update could be performed with the estimates obtained from the visual odometry. The visual odometry estimates are calculated at lower time intervals (in the range of a seconds) compared to the filter estimates (in the range of milliseconds). Therefore every time the visual odometry estimates are available, they could be used to correct the drifting estimates from the filter.

Bibliography

J. B. Balaram. Kinematic state estimation for a mars rover. In *Robotica*, volume 18, pages 251–262. Cambridge University Press, 2000.

A. Cross, A. Ellery, and A. Qadi. Estimating terrain parameters for a rigid wheeled rover using neural networks. *Journal of Terramechanics*, 50:165–174, June 2013.

M. Doumiati, A. Victorino, and A. Charara. An estimation process for vehicle wheel-ground contact normal forces. *IFAC Proceedings Volumes*, 41(2):7110 – 7115, 2008. 17th IFAC World Congress.

S. Hutangkabodee, Y. H. Zweiri, L. D. Seneviratne, and K. Althoefer. Soil parameter identification for wheel-terrain interaction dynamics and traversability prediction. *International Journal of Automation and Computing*, 3(3):244–251, July 2006.

K. Iagnemma and S. Dubowsky. Vehicle wheel-ground contact angle estimation: with application to mobile robot traction control. *Proceedings of the 7th International Symposium on Advances in Robot Kinematics, Piran-Portoroz, Slovenia, June*, 2000a.

K. Iagnemma and S. Dubowsky. Mobile robot rough-terrain control (rtc) for planetary exploration. In *Proceedings of the 26th Biennial Mechanisms and Robotics Conference of the 2000 ASME Design Engineering Technical Conferences*, September 2000b.

K. Iagnemma, A. Rzepniewski, S. Dubowsky, P. Pirjanian, T. Huntsberger, and P. Schenker. Mobile robot kinematic reconfigurability for rough terrain. volume 4196, pages 4196 – 4196 – 8, 2000.

K. Iagnemma, H. Shibly, A. Rzepniewski, and S. Dubowsky. Planning and control algorithms for enhanced rough-terrain rover mobility. In *6th International Symposium on Artificial Intelligence and Robotics Automation in Space: i-SAIRAS 2001*, June 2001.

K. Iagnemma, A. Rzepniewski, S. Dubowsky, and P. Schenker. Control of robotic vehicles with actively articulated suspensions in rough terrain. *Autonomous Robots*, 14(1):5–16, January 2003.

K. Iagnemma, S. Kang, H. Shibly, and S. Dubowsky. Online terrain parameter estimation for wheeled mobile robots with application to planetary rovers. *IEEE Transactions on Robotics*, 20(5):921–927, October 2004.

S. J. Julier and J. K. Uhlmann. New extension of the kalman filter to nonlinear systems. In *Int. Symp. Aerospace/Defense Sensing, Simul. and Controls. Signal Processing, Sensor Fusion, and Target Recognition*, volume 3068, pages 3068 – 3068 – 12, 1997.

G. Junlong, D. Liang, and G. e. a. Haibo. Longitudinal skid model for wheels of planetary rovers based on improved wheel sinkage considering soil bulldozing effect. *Journal of Terramechanics*, 74:45 – 56, 2017.

R. E. Kalman. A new approach to linear filtering and prediction problems. *Transactions of the ASME, Journal of Basic Engineering*, 82:35–45, 1960.

L. Kneip, D. Scaramuzza, and R. Siegwart. On the initialization of statistical optimum filters with application to motion estimation. In *Preoceedings IEEE/RSJ International Conference on Intelligent Robots and Systems*, pages 1500–1506, 2010.

A. C. Leite, A. Gallina, and B. Schäfer. Parameter identification and contact modeling for planetary wheeled rovers in soft soil. *IFAC Proceedings Volumes*, 45(16):1707 – 1712, 2012. 16th IFAC Symposium on System Identification.

Y. Li, L. Ding, Z. Zheng, Q. Yang, X. Zhao, and G. Liu. A multi-mode real-time terrain parameter estimation method for wheeled motion control of mobile robots. *Mechanical Systems and Signal Processing*, 104:758 – 775, 2018.

S. Marcel J. *Spacecraft Dynamics and Control : A practical engineering approach*. Cambridge University Press, 1997.

P. S. Maybeck. *Stochastic Models, Estimation and Control*, volume 1. New York: Academic Press, 1979.

P. Muir and C. Neuman. Kinematic modeling for feedback control of an omnidirectional wheeled mobile robot. In *Proceedings IEEE International Conference on Robotics and Automation*, volume 4, pages 1772–1778, March 1987.

N. Patel, R. Slade, and J. Clemmet. The exomars rover locomotion subsystem. *Journal of Terramechanics*, 47(4):227 – 242, 2010.

T. Peynot and S. Lacroix. Enhanced locomotion control for a planetary rover. In *Proceedings IEEE/RSJ International Conference on Intelligent Robots and Systems*, pages 311–317, October 2003.

L. E. Ray. Estimation of terrain forces and parameters for rigid-wheeled vehicles. *IEEE Transactions on Robotics*, 25(3):717–726, June 2009.

G. Reina, A. Milella, and F. W. Panella. Vision-based wheel sinkage estimation for rough-terrain mobile robots. In *15th International Conference on Mechatronics and Machine Vision in Practice*, pages 75–80, December 2008.

G. Saridis. Parameter estimation: Principles and problems. *IEEE Transactions on Automatic Control*, 28(5):634–635, May 1983.

B. Siciliano and O. Khatib. *Springer Handbook of Robotics*. Springer-Verlag, 2008.

D. Stavens and S. Thrun. A self-supervised terrain roughness estimator for off-road autonomous driving. *CoRR*, abs/1206.6872, 2012.

M. Tarokh and G. McDermott. Kinematics modeling and analyses of articulated rovers. *IEEE Transactions on Robotics*, 21(4):539–553, August 2005.

M. Tarokh and G. McDermott. A systematic approach to kinematics modeling of high mobility wheeled rovers. In *Proceedings IEEE International Conference on Robotics and Automation*, pages 4905–4910, April 2007.

O. Toupet, J. Biesiadecki, and A. Rankin. Traction control design and integration onboard the mars science laboratory curiosity rover. In *Proceedings IEEE International Aerospace Conference*, 2018.

E. A. Wan and R. Van Der Merwe. *Kalman Filtering and Neural Networks*. Wiley, 2001.

G. Welch and G. Bishop. An introduction to the kalman filter. In *Department of Computer Science , University of North Carolina at Chapel Hill*, July 2006.

J. Wendel. *Integrierte Navigationssysteme: Sensordatenfusion, GPS und Inertiale Navigation*. Oldenbourg, 2007.